Molecular Therapy
Original Article

Suppression of Zika Virus Infection in the Brain by the Antiretroviral Drug Rilpivirine

Ilker Kudret Sariyer,[1] Jennifer Gordon,[1] Tricia H. Burdo,[1] Hassen S. Wollebo,[1] Eleonora Gianti,[2] Martina Donadoni,[1] Anna Bellizzi,[1] Stephanie Cicalese,[1] Regina Loomis,[1] Jake A. Robinson,[1] Vincenzo Carnevale,[2] Joseph Steiner,[3] Mehmet H. Ozdener,[4] Andrew D. Miller,[5] Shohreh Amini,[1] Michael L. Klein,[2] and Kamel Khalili[1]

[1]Department of Neuroscience, Center for Neurovirology, Lewis Katz School of Medicine at Temple University, 3500 N. Broad Street, Philadelphia, PA 19140, USA; [2]Department of Chemistry, Institute for Computational Molecular Science, College of Science and Technology, Temple University, 1901 N. 12th Street, Philadelphia, PA 19122, USA; [3]Translational Neuroscience Center, National Institute of Neurological Disorders and Stroke, NIH, Bethesda, MD 20892, USA; [4]Monell Chemical Senses Center, 3500 Market Street, Philadelphia, PA 19104, USA; [5]College of Veterinary Medicine, Cornell University, T5-006A Veterinary Research Tower, Ithaca, NY 14853, USA

Zika virus (ZIKV) infection is associated with microcephaly in neonates and Guillain-Barré syndrome in adults. ZIKV produces a class of nonstructural (NS) regulatory proteins that play a critical role in viral transcription and replication, including NS5, which possesses RNA-dependent RNA polymerase (RdRp) activity. Here we demonstrate that rilpivirine (RPV), a non-nucleoside reverse transcriptase inhibitor (NNRTI) used in the treatment of HIV-1 infection, inhibits the enzymatic activity of NS5 and suppresses ZIKV infection and replication in primary human astrocytes. Similarly, other members of the NNRTI family, including etravirine and efavirenz, showed inhibitory effects on viral infection of brain cells. Site-directed mutagenesis identified 14 amino acid residues within the NS5 RdRp domain (AA265-903), which are important for the RPV interaction and the inhibition of NS5 polymerase activity. Administration of RPV to ZIKV-infected interferon-alpha/beta receptor (IFN-A/R) knockout mice improved the clinical outcome and prevented ZIKV-induced mortality. Histopathological examination of the brains from infected animals revealed that RPV reduced ZIKV RNA levels in the hippocampus, frontal cortex, thalamus, and cerebellum. Repurposing of NNRTIs, such as RPV, for the inhibition of ZIKV replication offers a possible therapeutic strategy for the prevention and treatment of ZIKV-associated disease.

INTRODUCTION

Zika virus, also called ZIKV, is an arthropod-borne arbovirus that has captured much attention in recent years due to its global spread by mosquitoes that caused an epidemic and its established association with congenital microcephaly in newborns and Guillian-Barré disease in adults.[1–7] ZIKV is a neurotropic virus that has been repeatedly isolated from newborns with clinical symptoms consistent with ZIKV infection and from brain autopsies of affected individuals.[8–10] While the pathology of the affected brain demonstrates massive neuronal cell injury and dropout, the role of the other cell types, including astrocytes, in supporting propagation of the virus in brain remains to be determined.[11–13]

The genome of ZIKV comprises a single positive-strand RNA of about 10.79 kb in size that, immediately after infection, appears in the cytoplasm and translates into a single polyprotein with a unique long open reading frame (ORF). The ORF encodes for all of the three structural protein genes, including Capsid-C, pre-Membrane-prM, and Envelope-E, from the 5′ regions of the genomic RNA. The 3′ portion of the RNA is responsible for expression of the seven nonstructural protein genes: NS1, NS2A, NS2B, NS3, NS4A, NS4B, and NS5.[14] Replication of ZIKV initiates with the synthesis of a negative-strand RNA that serves as a template for the production of positive-strand RNA. NS5, with its RNA-dependent RNA polymerase (RdRp) activity, is critically important for the production of both positive and negative strands of ZIKV RNA during the infection cycle.[15] In this proof-of-concept study, we provide evidence that a family of non-nucleoside reverse transcriptase inhibitors (NNRTIs), including rilpivirine (RPV), by targeting NS5 strongly suppresses ZIKV replication *in vitro* and alters the preclinical outcome *in vivo* in the ZIKV-infected experimental animals.

RESULTS

Effect of Reverse Transcriptase Inhibitors on ZIKV Infection

As a first step to investigate the biological effect of reverse transcriptase inhibitors on ZIKV, we examined the ability of primary cultures of human fetal and adult astrocytes (PHFAs and PHAAs, respectively) as well as several other cell types, including primary culture of human fetal microglia and fetal neurons (PHFMs and PHFNs, respectively) and human neuroprogenitor cells (NPCs), in supporting ZIKV infection. Results showed a dramatically higher level of ZIKV

Received 13 July 2019; accepted 4 October 2019;
https://doi.org/10.1016/j.ymthe.2019.10.006.

Correspondence: Kamel Khalili, PhD, Department of Neuroscience, Center for Neurovirology, Lewis Katz School of Medicine at Temple University, 3500 N. Broad Street, 7th Floor, Philadelphia, PA 19140, USA.
E-mail: kamel.khalili@temple.edu

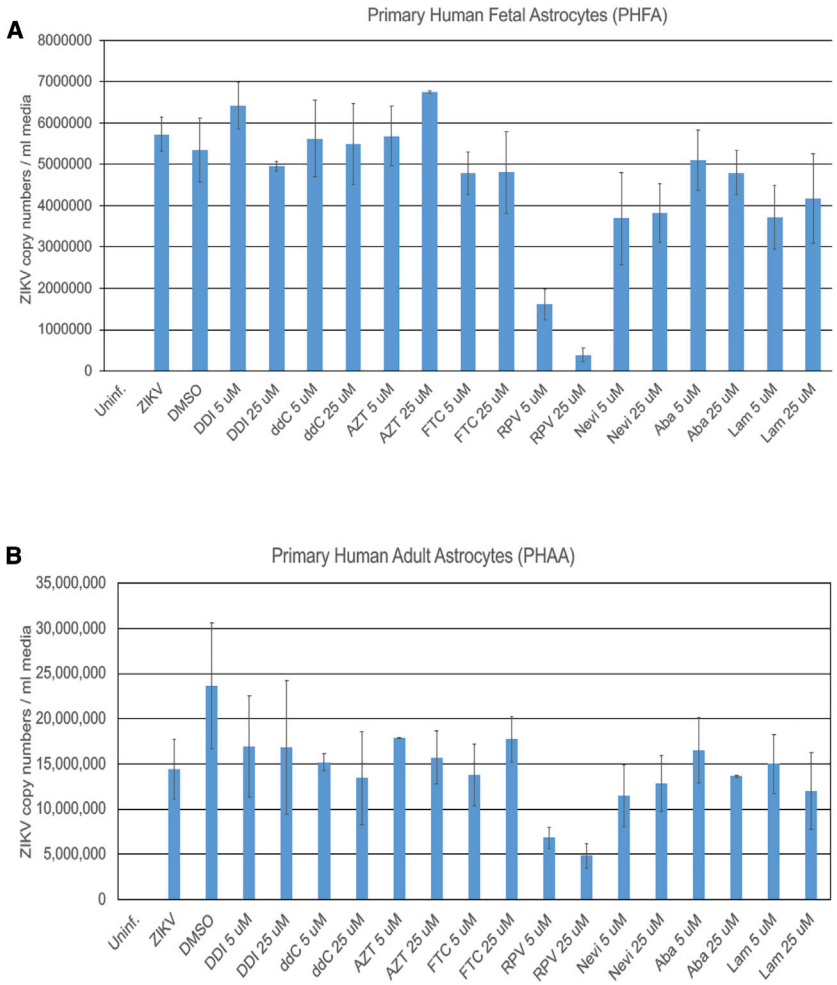

Figure 1. Effect of NRTIs and NNRTIs on ZIKV Propagation in Primary Human Fetal and Adult Astrocytes

Primary human fetal (A) and adult (B) astrocytes were infected with the PRVABC597 strain of ZIKV. Cells were also treated with several nucleoside and non-nucleoside reverse transcriptase inhibitors at 5- and 25-μM concentrations. At 3 dpi, growth media of the cells were collected and analyzed by real time qRT-PCR and are shown as bar graphs. DDI, didanosine; ddC, dideoxycytidine; FTC, emtricitabine; AZT, zidovudine; Nevi, nevirapine; RPV, rilpivirine; Aba, abacavir; Lam, lamivudine.

infection of PHFAs and PHAAs compared to any other cell types used in this study (Figure S1).

Next, we used these two cell types for further studies, and we observed that, under identical conditions, among the eight distinct members of nucleoside reverse transcriptase inhibitors (NRTIs) and NNRTIs tested in this study, only the NNRTI RPV exhibits a profound ability in suppressing ZIKV infection in both PHFA and PHAA cells (Figure 1). Further studies verified the inhibitory effects of RPV, but not of inhibitors in the NRTI class, including lamivudine (LAM) and abacavir (ABA), on the intracellular level of ZIKV RNA sequences corresponding to NS2A and NS4A genes (Figure S2A). Accordingly, the level of viral capsid protein was found undetectable in the ZIKV-infected cells after treatment with RPV, but not with LAM and ABA (Figure S2B). Moreover, results from western blot analysis revealed a dose-dependent inhibitory effect of RPV on ZIKV production of proteins NS1, NS3, and NS5 (Figures S3A–S3D). Dose effect assessments on naive cells revealed that RPV did not alter cellular viability at up to 25 μM concentrations (Figure S4). Collectively these observations demonstrated that RPV has a potential to control ZIKV replication in human brain cell cultures.

Assessment of RPV Binding to ZIKV NS5 via Computation

To gain insight into the mechanism of RPV inhibition of ZIKV replication, first we focused on NS5, an essential viral protein that plays key roles in the life cycle and survival of the virus. The structure of ZIKV NS5 comprises two domains: an N terminus methyltransferase (MTase) domain, responsible for methylation at the viral RNA cap site, and a C terminus RdRp domain, which synthesizes the viral RNA.[16,17] The MTase domain comprises two adjacent binding sites, one for the S-adenosyl-L-methionine (SAM) methyl donor (SAM site) and the other for 7-methyl guanosine diphosphate (^{m7}Gpp) substrate (cap site) (Figure 2; Figures S5 and S6). The RdRp domain features a very large site to accommodate the genome RNA (palm site). The palm site is located at the interfaces of structural features that constitute the hallmarks of the RdRp protein domain, i.e., the palm, fingers, and thumb sub-domains (Figures S5–S8). The majority of the available ZIKV-NS5 structures only comprise either the MTase (apo or bound to substrate/cofactor ligands) or the RdRp domains (apo).

We selected two nearly full-length structures of ZIKV NS5 (PDB: 5TMH and 5TFR),[17,18] and we performed a computational search for druggable sites suitable to accommodate small molecule ligands, including the NNRTI RPV and etravirine (ETR). Our results indicate that the structure of ZIKV NS5 features five potentially druggable sites, suitable for the binding of fragment- or drug-like molecules (Figure 2). In particular, the MTase domain (pink) comprises a druggable spot that extends over both the SAM site and the cap site. Instead, in addition to two small, lateral binding spots, the RdRp domain (light blue) features a very large site, named the palm site, lying in the center of the palm sub-domain.

We explored, by computational docking, the possibility of RPV binding to the top three druggable sites of NS5 (prioritized by considering

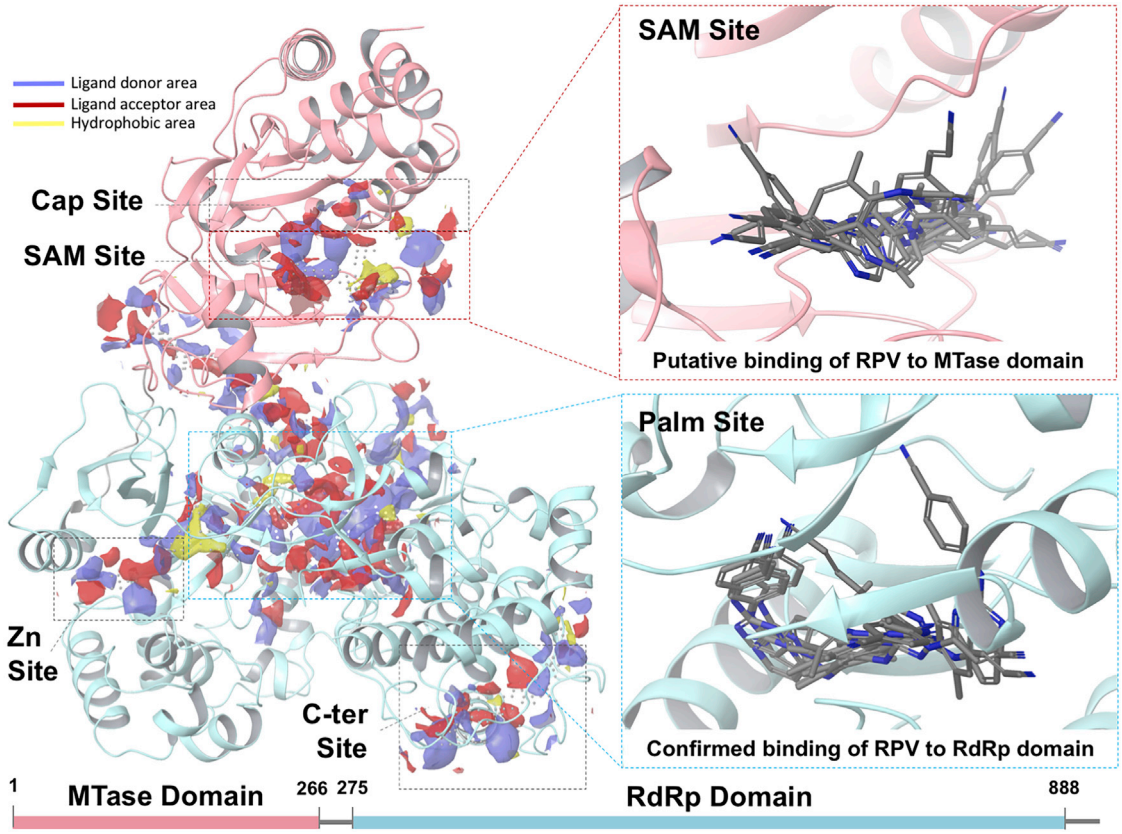

Figure 2. Computational Assessment of RPV Binding to ZIKV NS5

Structural features of ZIKV NS5 and its potential interaction sites with RPV were characterized via computation. The structure of ZIKV NS5 is shown in new cartoon representation. The MTase and RdRp domains are colored in pink and light blue, respectively. Left panel: druggable sites are shown as site maps (yellow, hydrophobic surface; red, ligand acceptor surface; and blue, ligand donor surface). Right panels: zoom-in of the SAM site (top panel) and the palm site (bottom panel). For each site, top scoring binding modes of RPV are shown.

Dscore[19] and by their ability to bind known ligands), namely, the cap site, SAM site (MTase domain), and palm site (RdRp domain). Due to a poor docking score, we promptly excluded the hypothesis that RPV could bind at the cap site. However, docking results alone could not rule out RPV binding to the other two locations, namely, the SAM and the palm sites. Representative binding modes of RPV to NS5 are shown in Figure 2 (right panels). Furthermore, for each site, the best binding modes of RPV are shown in Figures S5–S9. Binding of RPV at the SAM site (MTase domain) superimposed very well with that of the SAM ligand, involving critical residues required for its binding (i.e., H110) (Figure S5). Moreover, RPV overlaps nicely with site maps of complementary chemical features: while the benzonitrile moiety extends over a large hydrophobic area of the receptor (yellow map), the terminal cyanovinyl group points toward the ligand acceptor map (red map).

Binding at the large palm site represented also a viable hypothesis, as suggested by our computational modeling (Figures S6–S9) and partially supported by experimental evidence of HIV-1 reverse transcriptase (RT) structures in complex with RPV and ETR.[20,21] Indeed, both RPV and ETR are known to bind, in a similar fashion as suggested by our modeling, at the palm domain of HIV-1 RT, thereby disrupting the RT polymerase function allosterically. Our computational studies suggested that RPV shows promiscuous binding preferences at the palm site (RdRp domain), with docking poses distributed into three main clusters. In all cases, RPV binds in the proximity of the Priming Loop (PL) feature, but with different orientations: toward the fingers (finger sub-pocket), the palm (palm sub-pocket), or the thumbs (thumb sub-pocket) (Figure S6D). Each binding hypothesis finds experimental counterparts with Dengue virus (DENV) NS5 RdRp structures, apo or co-crystallized with known ligands.[16,22–24] Interestingly, in all three cases, RPV is predicted to adopt a horseshoe-like conformation, typical of RPV binding to HIV-1 RT.[20,21]

Furthermore, in an attempt to predict the bioactive conformations of RPV and ETR, we conducted a search for low-energy conformers of these molecules using a procedure described by Watts et al.[25] As for RPV, our studies predicted two clusters of possible bioactive conformations. The most stable conformers adopted a horseshoe shape, similar to binding modes of RPV in all the sub-pockets at the RdRp

domain and nearly identical to those of the palm sub-pocket at the RdRp domain. Additionally, a second cluster of putative bioactive conformers of RPV was predicted to adopt an extended conformation, similar to that of binding modes at the SAM site (Figure 2; Figure S5). Instead, only one cluster of bioactive conformers was obtained for ETR, which interestingly adopted the horseshoe conformation. Of note, experimental structures of RPV in complex with HIV-1 RT[20,21] indicate that, upon binding, the ligand adopts a conformation, i.e., the horseshoe shape, strikingly similar to our predictions. Taken together, these observations suggested that binding of RPV (and possibly ETR) likely occurs at the palm site (RdRp domain) of NS5. To further corroborate our findings, we computationally selected a set of NS5 amino acid residues, located on the RdRp domain, for experimental mutagenesis and drug-binding studies. These experiments supported the hypothesis that RPV binds at the RdRp domain and ruled out the possibility that binding occurs at the SAM site.

Interplay of RPV with NS5 and Inhibition of ZIKV Replication in Human Brain Cells

To assess interactions of RPV with NS5 protein, we employed differential scanning fluorimetry (DSF) known as protein thermal shift assays.[26–28] We determined that PBS at pH 7.4 (physiologic conditions) usage resulted in reproducible protein melting temperatures (Tm). Upon incubation of NS5-MBP with increasing concentrations of RPV, we observed a concentration-dependent right shift in Tm of about 1°C with 3–10 μM RPV, with an apparent binding affinity of 100 nM (Figure 3A, left). The observed interactions of RPV with NS5 protein were specific to NS5 and not the MBP fusion vehicle, since purified MBP alone exhibited no shift in Tm upon incubation with RPV (Figure 3A, right). Results from the polymerase assay demonstrated that RPV profoundly interfered with the NS5 polymerase activity and, under a similar condition, azidothymidin (AZT), a known NRTI, had no effect on the NS5 activity (Figure 3B). Again, while treatment of the infected cells with AZT had no effects on the ZIKV replication of PHFA, RPV showed a profound inhibitory effect on ZIKV infection of the cells (Figure 3C). Accordingly, computational docking of AZT to the investigated druggable sites of NS5 resulted in a poor predicted binding (Figure S11).

We also evaluated the effect of two other members of NNRTIs that are closely related to RPV, including ETR and efavirenz (EFA),[29] on the ZIKV replication and viral protein production. As shown in Figure 3D, while at 25 μM all three drugs effectively suppressed viral load in the cultured media and inhibited viral capsid production (Figure 3E), the inhibitory effect of RPV and ETR was detected at the lower concentrations of the drugs, a behavior supported by computational investigations (Figures S10 and S11).

To determine the kinetics of ZIKV replication and the effect of RPV on the viral propagation, real-time qRT-PCR was performed. Replication of ZIKV, as determined by the viral RNA copy numbers, was initiated at 1 day post-infection, peaked at day 3, and sharply declined thereafter and remained at very low but detectable levels until day 10 post-infection (Figure 3F). Daily treatment of the infected cells with RPV prevented the burst of the viral replication at day 3 and kept the replication of ZIKV at an undetectable level during the course of our study. Interestingly, interruption of the RPV treatment at day 4 post-infection caused no rebound in the virus production during the remaining course of the 10-day experiment (Figure 3F). This observation rules out the emergence of mutant virus that may escape from the inhibition imposed by RPV. Treatment of the infected cells with various concentrations of RPV that effectively suppressed viral replication improved the cell viability and/or restored cell proliferation (Figure 3G). Examination of viral replication in primary culture of human fetal brain astrocytes by immunocytochemistry showed the presence of NS1 in the cells expressing astrocytic cell marker protein glial fibrillary acidic protein (GFAP) and their absence upon the treatments with RPV, but not AZT (Figures 3H and 3I).

Interaction of RPV with NS5 and Its Effects on Enzymatic Activity

To gain more insight into the RPV binding to NS5 and its impact on polymerase activity of the protein, we selectively mutated 14 amino acid residues to alanine within the palm region of the protein that possesses potential binding affinity to RPV, as predicted by our computational modeling (Figures 4A and 4B; Figures S10 and S11). NS5 mutant proteins were recombinantly synthesized, purified, and utilized for a thermal shift assay and RNA polymerase assays in the presence or absence of RPV. The results did rule out any involvement of MTase domain of NS5, located in the N terminus of the protein, in binding to RPV (Figure 4C). Accordingly, these results confirmed that RNA polymerase activity of wild-type RdRp NS5 (C terminus) is dramatically affected by the presence of RPV (Figure 4D). Interestingly, the mutant construct carrying mutations in 14 amino acid residue positions, as identified by the computational modeling (NS5-RdRp mutant-14A), maintained RNA polymerase activity, although at reduced capacity, when compared to the truncated wild-type protein. In the presence of RPV, RNA polymerase activity was only mildly alleviated, in agreement with RPV-binding affinity studies that detected no binding to the mutated construct. Loss of experimental binding affinity, in conjunction with enzymatic activity at almost full capacity, suggested that one or more amino acid residues mutated in the 14A construct are critical for RPV binding.

Binding affinity of AZT to the RdRp-wild-type (WT) and RdRp mutant domains was also analyzed by thermal shift assay, and the results indicated that the Tm was not changed in a concentration-dependent manner, so no significant binding of AZT to these proteins was observed (data not shown).

To further determine and characterize selective anti-ZIKV activity of RPV, we utilized the RdRp-14A protein, which showed a comparable polymerase activity but no significant binding to RPV. RdRp-14A was cloned into a mammalian expression vector and transiently transfected into primary human astrocytes. The cells were then infected with ZIKV in the presence and absence of RPV and analyzed by qRT-PCR for viral replication. As expected, ZIKV infection was

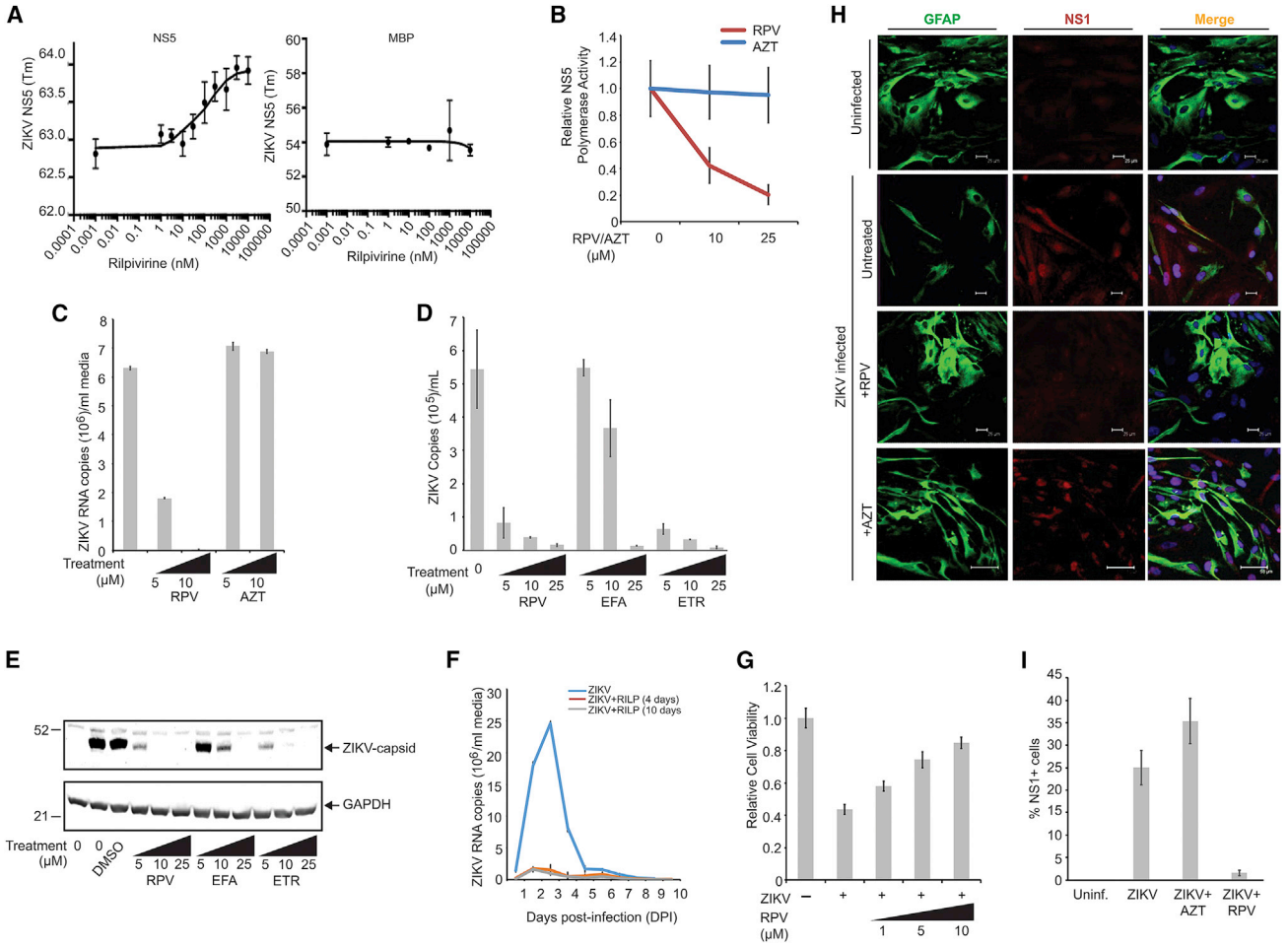

Figure 3. Inhibition of ZIKV Infection of Human Primary Culture of Brain Cells by RPV

(A) Interaction of ZIKV NS5 protein with RPV using protein thermal shift assays. The relative fluorescence emitted by the thermal shift dye is recorded during the temperature ramp phase and plotted versus temperature (left panel). Tm value was calculated from the derivative of the thermal melt curves and plotted as effects of various concentrations of RPV, as described in the Materials and Methods. Determination of binding interaction of maltose binding protein (MBP) moiety of NS5-MBP with RPV using differential scanning fluorimetry (DSF) showed no association of MBP with RPV (right panel). (B) RPV inhibits RNA polymerase activity of ZIKV NS5 protein. 1 μg ZIKV RNA and 500 ng recombinant NS5 protein were added to the reaction buffer, in the presence and absence of RPV or AZT at 10- or 25-ng concentration, and analyzed as described in the Materials and Methods. Relative NS5 activity was calculated from three independent experiments and is shown as a trend-line graph. (C) PHFA cells were infected with ZIKV (0.5 plaque-forming unit [PFU]). Cells were treated daily with increasing concentrations of RPV and AZT (5 and 10 μg/mL). At 3 dpi, ZIKV RNA copies in the growth media were analyzed by real time qRT-PCR and are shown as a bar graph. (D) PHFA cells were infected with ZIKV (0.1 PFU). Cells were treated daily with increasing concentrations of RPV, EFA, and ETR (5, 10, and 25 μg/mL). At 3 dpi, ZIKV RNA copies in the growth media were analyzed by real time qRT-PCR and are shown as a bar graph. (E) Whole-cell protein extracts were also prepared from the same set of experiments from (D) and analyzed by western blotting for the detection of ZIKV capsid protein. GAPDH (glyceraldehyde-3-phosphate dehydrogenase) was probed in the same membranes and is shown as a loading control. (F) PHFA cells were divided into three groups. The first group was infected with ZIKV and mock treated at 24-h intervals for 10 days. The second group of cells was infected with ZIKV (0.1 PFU) and treated with RPV (5 μg/mL) at 24-h intervals for only 4 days. The third group was also infected with ZIKV (0.1 PFU) and treated with RPV (5 μg/mL) at 24-h intervals for 10 days. The growth media of cells were collected every day, starting from 1 dpi up to 10 dpi, and analyzed by real time qRT-PCR. ZIKV viral loads were determined as ZIKV RNA copies per milliliter culture media and are shown as a trend-line graph for each group. (G) PHFAs were infected with ZIKV (0.1 PFU) and treated with RPV at 1-, 5-, and 10-μg/mL concentrations for 4 days. PHFA cell viability was analyzed by MTT (3-(4,5-dimethylthiazol-2-yl)-2,5-diphenyltetrazolium bromide) assay and is shown as a bar graph from three independent experiments. (H) PHFA cells were infected with ZIKV (0.1 PFU) and treated daily with RPV and AZT. At 4 dpi, cells were fixed and processed by immunocytochemistry for the detection of cellular GFAP (green) and viral NS1 (red) proteins, as described in the Materials and Methods. (I) DAPI-positive and NS1-immunoreactive cells from studies shown in (H) were counted in at least three different stainings of the conditions using Photoshop, and percentages of NS1 cells were graphed.

greatly suppressed by RPV in control infections. On the other hand, co-expression of the RdRp-14A protein in ZIKV-infected cells was able to recover RPV-mediated suppression of ZIKV replication (Figure 4E). These results further suggest that RdRp-14A mutant is enzymatically active in cells and able to complement the RPV-mediated suppression of the wild-type RdRp functions.

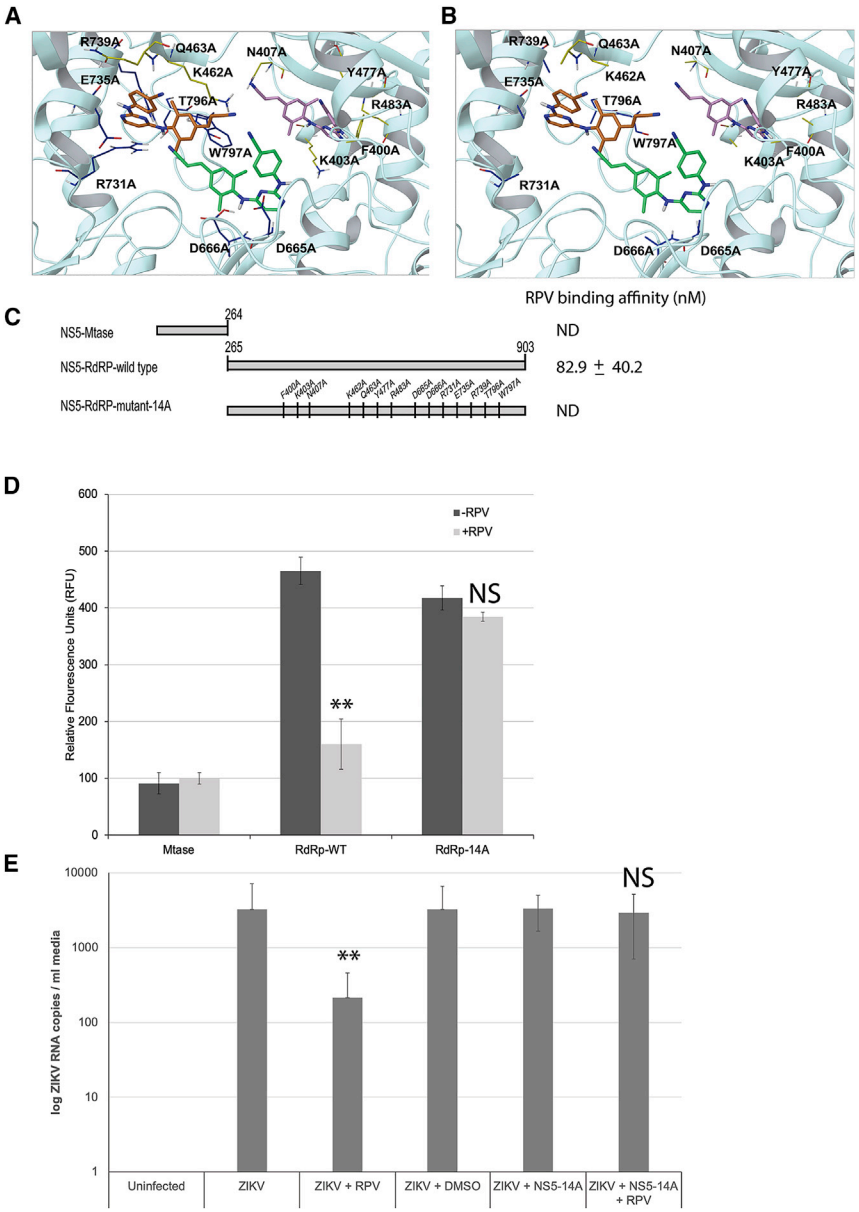

Figure 4. Physical and Functional Assessment of RPV Binding to NS5 Mutants with Site-Directed Mutagenesis

Structural features of ZIKV NS5-RdRp wild-type (A) and NS5-RdRp mutant-14A (B) and their potential interaction with RPV were characterized via computation. In both wild-type (A) and mutant-14A (B) panels, side chains are color coded by NS5 mutant (yellow or blue for mutant-N7A or mutant-C7A, respectively). Binding modes are ranked by docking score (kcal/mol): −7.4 (best predicted binding), −6.6, and −5.6 for RPV poses in green, orange, and pink carbons, respectively. The bottom ranking pose (pink carbons) is obtained for RPV interacting with mutant-N7 residues and shows no binding; hence, this binding mode (pink carbon RPV) is less likely to occur. (C) Schematic presentation of amino acid mapping of NS5 wild-type and side-directed mutations (14A) are illustrated. The relative fluorescein emitted by the thermal shift dye is recorded during the temperature ramp phase and plotted versus temperature. ND denotes no significant affinity detection. (D) Effect of RPV on RNA polymerase activities of MTase domain and RdRp wild-type and RdRp-14A proteins was also analyzed by RdRp assay. 1 μg ZIKV RNA and 500 ng recombinant NS5 full-length or mutant proteins were added to the reaction buffer in the presence and absence of RPV (10 ng) and analyzed as described in the Materials and Methods. NS5 activity was calculated from three independent experiments and quantified as relative fluorescence units (RFU) emitted during the reaction. (E) ZIKV RdRp-14A mutant was cloned into a mammalian expression vector. PHFA cells were transiently transfected with this construct and either treated with RPV or left untreated. Cells were infected with ZIKV (0.1 PFU) at 24 h post-transfections, and growth media of cells were analyzed by qRT-PCR for ZIKV RNA copies. **$p < 0.05$.

RPV Suppresses ZIKV Infection in IFN$^{-/-}$ Mice and Changes the Preclinical Outcome

To extend our *in vitro* results, we established an *in vivo* mouse model of ZIKV infection. Interferon receptor (IFNR)-knockout (IFNR$^{-/-}$) mice (n = 6) were infected with the Puerto Rico (PRVABC59) strain of ZIKV through footpad injections.[30] Three of these animals were also treated with RPV (ZIKV + RPV) in order to explore the utility of RPV as an anti-viral agent for ZIKV *in vivo*. The control group was uninfected mice treated with RPV (uninfected RPV only, n = 3). In a second set of experiments, results from these studies were validated using a larger cohort of animals in each group (n = 6; Figure S12). All mice were monitored daily for survival and signs of disease with bi-daily weight monitoring and daily grasp test analysis. Physical, behavioral, and motor coordination/paralysis inspections were also performed at the time of weight checks bi-daily.

Both sets of ZIKV-infected animals lost weight (Figures 5A and S12A); however, the RPV-treated ZIKV-infected animals recovered. There was no significant weight loss in the RPV-only animals. Clinical scores (as measured by grasp test and physical assessment) in ZIKV-infected animals were increased after infection. The animals treated with RPV returned to baseline levels where the untreated animals continued to progress with poor clinical scores (Figure 5B; Figure S12B). Mice were sacrificed based on weight loss and physical, behavioral, and motor function deficits. One ZIKV-infected animal was sacrificed at 7 days post-infection (dpi) and two others at 8 dpi, suggesting that ZIKV infection is highly lethal in IFNR$^{-/-}$ mice (Figure 5C). In the second set of studies, all six ZIKV-infected animals were sacrificed at 8 dpi (Figure S12C). On the other hand, all mice from ZIKV-infected and RPV-treated groups survived until

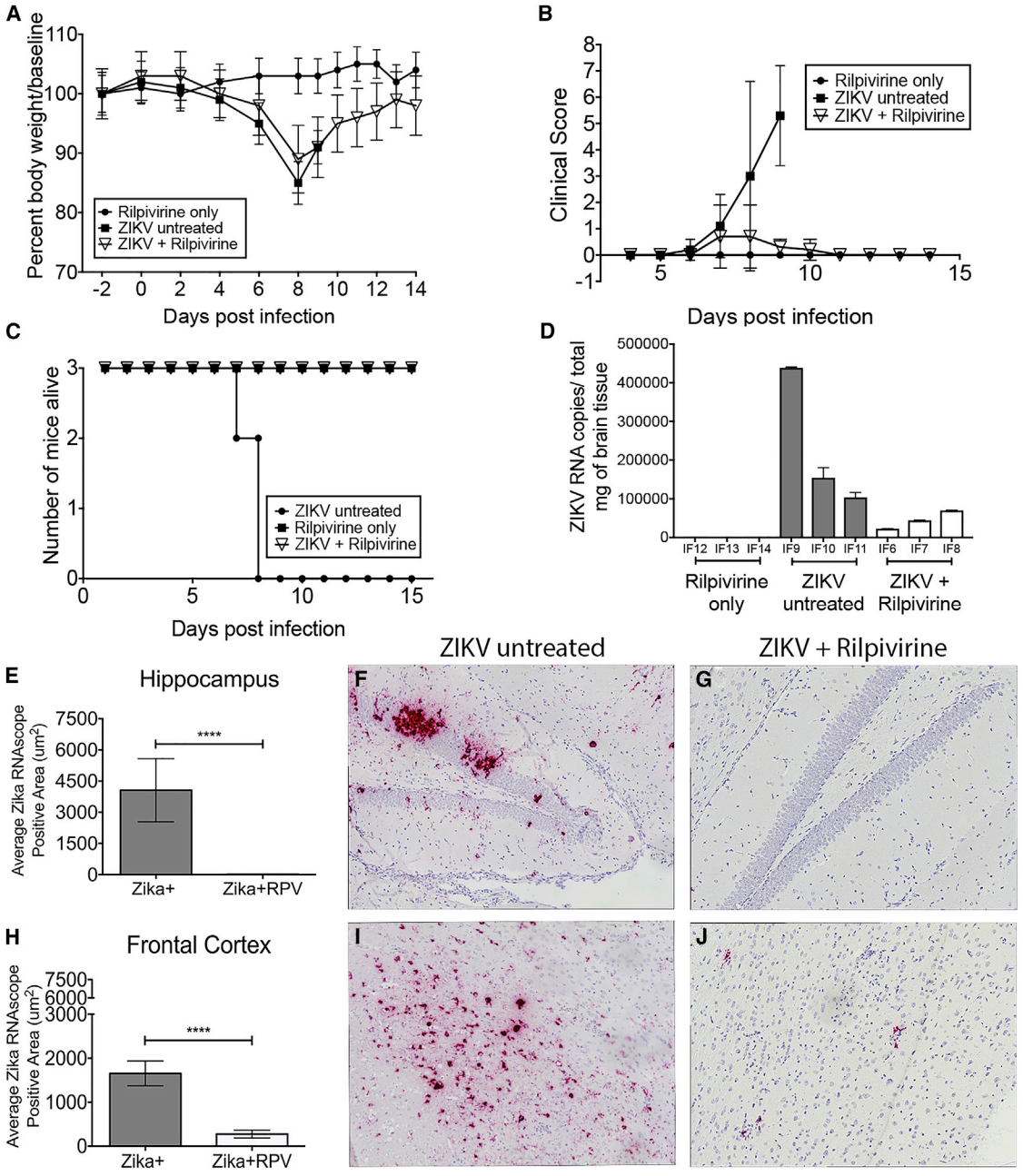

Figure 5. RPV Inhibits ZIKV Propagation, Reverses the Mortality, and Decreases the Viral Burden in the Brain of IFNR$^{-/-}$ Mice

(A) Body weights were measured for each mouse from the three groups (closed circle, rilpivirine only; closed square, ZIKV untreated; and open triangle, ZIKV + RPV) until the end of the study (14 days post-infection [dpi]). Data are shown as a percent of body weight compared to baseline. (B) Grasp tests were performed daily starting at 4 dpi and analyzed for clinical scoring for the three groups. (C) Survivor curve analysis is shown based on the Kaplan-Meier estimates. All animals in the uninfected + RPV and ZIKV-infected + RPV groups survived until the end of the study. The ZIKV-infected and untreated mice were sacrificed at 7 and 8 dpi. (D) ZIKV RNA copies per milligram total brain lysates are presented per animal (IF6–IF14). The mean and SD are shown, and the SD was calculated from triplicate analysis of the RNA samples from each mouse. (E–J) ZIKV RNA was visualized with RNAscope (red) and quantified in the hippocampus and the frontal cortex of ZIKV-infected untreated animals (ZIKV+) and ZIKV-, RPV-treated animals (ZIKV + RPV). (E) The average ZIKV+ RNA area in the hippocampus of the ZIKV-untreated (gray bars) mice compared to the ZIKV + RPV group (white bars) showed a significant reduction in the ZIKV RNA with RPV ($p < 0.0001$). (F) Representative image of hippocampus ZIKV RNAScope staining reveals high viral RNA signal in ZIKV mice. (G) Representative image of hippocampus ZIKV RNAScope staining shows significantly less signal in ZIKV + RPV mice. (H) The average ZIKV+ RNA area in the frontal cortex of the ZIKV-untreated (gray bars) mice compared to the ZIKV + RPV group (white bars) showed a significant reduction in the ZIKV RNA with RPV ($p < 0.0001$). (I) Representative

(legend continued on next page)

the end of the study (14 dpi), suggesting that RPV was capable of reversing ZIKV-associated mortality in this animal model.

At the end of the study, brain and peripheral organs (spleen, liver, kidney, and lung) were harvested for pathological analysis at necropsy. All brain regions (thalamus, hippocampus, frontal cortex, and cerebellum) examined in the ZIKV-only mice had significant inflammation, but also abundant apoptotic/necrotic cell damage, which has been described in other ZIKV-infected mouse models.[30–32] In the RPV-treated ZIKV-infected animals, there was still significant inflammation, but no apoptotic/necrotic cell damage was observed (Figure S13). The RPV-only control brains were unremarkable. Spleen, liver, kidney, and lung from all mice were unremarkable with no pathology (Figure S14).

ZIKV RNA copies in post-mortem brain were quantified in all animals by RT-PCR (Figure 5D). As expected, there were no ZIKV RNA copies detected in the RPV-only control animals. There were up to 400,000 copies of ZIKV RNA/mg of tissue detectable in the infected animals. The ZIKV RNA copies in the brain were significantly reduced in mice treated with RPV. To assess viremia in the specific regions of the brain of ZIKV mice, we utilized an RNAscope to detect Zika viral RNA in hippocampus and frontal cortex (Figures 5E–5J). The kidney, liver, lung (Figures S14A–S14F), spleen (Figures S14G–S14I), thalamus (Figures S14J–S14L), and cerebellum (Figures S14M–S14O) were also assessed for ZIKV RNA. Administration of RPV significantly decreased the amount of ZIKV RNA^+ cells in the hippocampus compared to ZIKV only (Figures 5E–5G; 4,061.5 ± 1,515.1 μm^2 versus 25.5 ± 12.4 μm^2, $p < 0.0001$). Similarly, in the frontal cortex there was a significant reduction in ZIKV RNA in mice treated with RPV (Figures 5H–5J; 1,653.3 ± 283.0 μm^2 versus 273.0 ± 89.0 μm^2, $p < 0.0001$). A significant decrease in ZIKV RNA was seen in the spleen, thalamus, and cerebellum (Figures S14G–S14O). There was very little to no virus seen in the kidney, liver, and lung (Figures S14A–S14F). Overall, RPV administration proved efficacious at preventing ZIKV infection in the brain, with a dramatic reduction of ZIKV RNA in the brain and spleen.

The *in vitro* data presented thus far have demonstrated ZIKV replication predominantly in astrocytes. To examine the specific CNS cell types infected by ZIKV *in vivo*, dual RNAscope for ZIKV RNA and subsequent immunohistochemistry for cell subpopulations were utilized. Co-localization was investigated in the hippocampus and frontal cortex preferentially due to the higher viral RNA in these two regions with ZIKV infection. As demonstrated *in vitro*, ZIKV RNA showed overlap with GFAP+ astrocytes in both the frontal cortex and hippocampus (Figures 6A and 6B). Virus was detected in both the cell body and in the astrocytic projections. Microglia and macrophages were detected using an antibody against IBA-1 and showed significant co-localization with ZIKV RNA (Figures 6C and 6D). T cell accumulation, visualized by CD3, in the brains of ZIKV-infected mice was noted compared to uninfected controls (data not shown). ZIKV RNA was detected in T cells in both the frontal cortex and the hippocampus (Figures 6E and 6F). Viral RNA showed co-localization with neurons in the frontal cortex, but, in the hippocampus, NeuN and viral RNA showed more proximity than overlap (Figures 6G and 6H). An antibody against nestin was used to examine the presence of progenitor cells in the frontal cortex and hippocampus. There were no nestin+ cells detected that contained ZIKV RNA (Figures 6I and 6J). Overall, these *in vivo* results show that the major cell populations infected in this model are astrocytes, inflammatory monocytes, and T cells and neurons.

DISCUSSION

Through a computational assessment of ZIKV NS5, we identified potential sites of interaction with the NNRT inhibitor RPV that may impact on the enzymatic activity of NS5, hence impairing a productive ZIKV infection cycle. In particular, we showed that NS5 features two druggable sites, both suitable for the binding of small molecule ligands, like RPV. The first one, the SAM site, is located on the MTase domain of NS5 (N terminus), and coincides with the binding pocket of SAM, the methyl donor in the 5′ RNA cap structure.[16] Therefore, the binding at this site of small molecules, such as RPV and ETR, would compromise allosterically viral replication. The second site, the palm site, is located on the RdRp domain of NS5 (C terminus) and overlaps with a ligand-binding pocket shared by DENV NS5 and conserved within the flavivirus family.[24] It has been shown that competitive binding at the palm site inhibits enzymatic activity of DENV RdRp.[24] We envision that a similar mechanism might be exerted by the binding of RPV (as well as by other NNRTIs, like ETR) at equivalent locations in ZIKV NS5.

Further studies, including the computationally guided experimental mutation of several amino acid residues with potential binding affinity for RPV, excluded the hypothesis that the MTase domain of NS5 (N terminus) is involved in binding to RPV. On the contrary, we found that RPV has an affinity for binding to the RdRp domain (AA265-903 strain) of the NS5 protein (C terminus). Interestingly, by introducing mutations of 14 amino acid residues (mutant-14A), as suggested by computational modeling, we showed that RPV interactions with the RdRp domain are significantly alleviated, a clear indication that RPV binding is mediated by one or more of the mutated residues. In addition, the results from the polymerase activity assay further corroborated with binding data, thereby suggesting that RPV interferes with NS5 polymerase activity by binding to its RdRp domain. Further computational work (i.e., extensive molecular dynamics simulations), combined with experimental mutagenesis and *in vitro* activity studies, will be required to characterize the

image of a frontal cortex ZIKV RNAScope *in situ* reveals high viral RNA signal in ZIKV mice. (J) Representative image of frontal cortex ZIKV RNAScope staining shows significantly less signal in ZIKV + RPV mice. The average ZIKV RNA signal area was quantitated as the average of 10, non-overlapping 40× images from each animal (n = 3/group), using a Keyence BZ-X700 microscope. Bar graphs show average ZIKV RNA area (mean, SEM). Comparison of means was determined by Mann-Whitney, two-tailed t test (*$p < 0.05$, ****$p < 0.0001$).

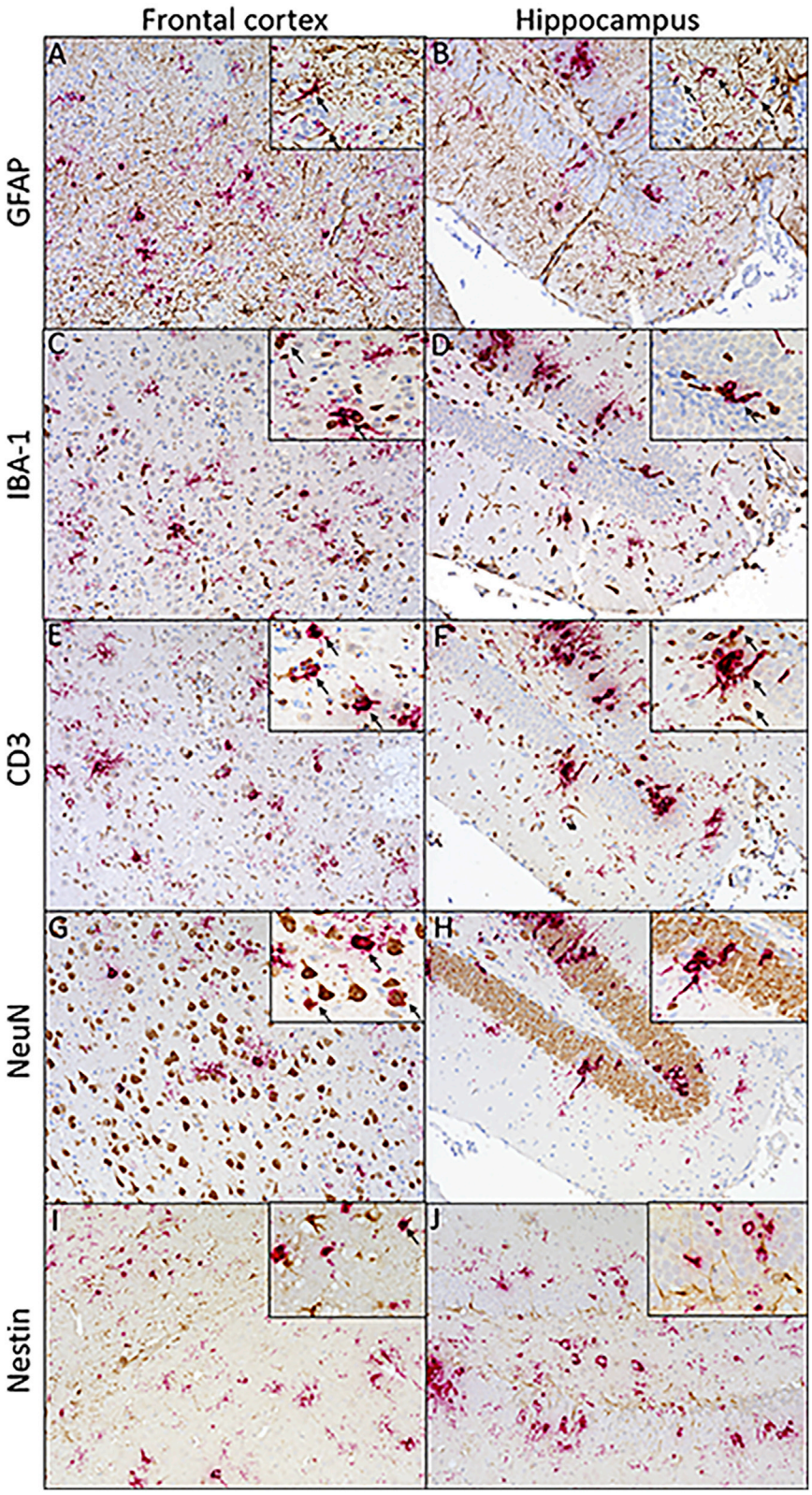

Figure 6. ZIKV RNA Co-localization with Astrocytes and Microglia/Macrophages

T cells, neurons, and progenitor cells in the frontal cortex and hippocampus. ZIKV RNA was visualized with RNAscope (red) and cell markers by immunohistochemistry (brown) in the frontal cortex and hippocampus of ZIKV-infected animals (ZIKV+). GFAP was used to visualize astrocytes in tissue. Astrocytes showed significant overlap with viral RNA in the frontal cortex and hippocampus. (A and B) IBA-1 served as a marker for microglia and macrophages in tissue. Microglia and macrophages showed co-localization with viral RNA both in the frontal cortex (A) as well as the hippocampus (B). (C and D) CD3 was used to characterize T cells in tissue, which showed co-localization with viral RNA in the frontal cortex (C) and the hippocampus (D). (E and F) Neuronal nuclear protein, NeuN, served as a marker for neurons in tissue. Viral RNA showed co-localization with neurons in the frontal cortex (E), but, in the hippocampus (F), NeuN and viral RNA showed more proximity than overlap. (G and H) No overlap of staining is seen with ZIKV RNA and nestin, a marker of progenitor cells: frontal cortex (G) and hippocampus (H). (I and J) Representative images were taken at 20× magnification with a Keyence BZ-X700 microscope: frontal cortex (I) and hippocampus (J). Magnified images were taken at 60× and arrows were used to denote double-positive cells.

structural details of the conformational transitions associated with ZIKV polymerase activity (so far largely unknown) and to fully elucidate the binding preferences of NNTIs to NS5, starting with RPV and ETR. Nonetheless, our current work offers a proof of concept that RPV can bind to ZIKV NS5, resulting in severe impairment of its activity, as shown in our study and viral RNA genome replication in a well-controlled cell culture model. Besides characterizing the presence of multiple druggable hotspots of ZIKV NS5 (both at the MTase and RdRp domains) that can be targeted by small molecule modulators, our studies, by highlighting the role played by the intrinsic plasticity of ZIKV NS5 into small molecule ligand binding, emphasize the importance of incorporating protein flexibility into drug discovery strategies.

To assess the *in vivo* impact of RPV on ZIKV infection, we then employed the IFN$^{-/-}$ mouse model that has been widely used to demonstrate ZIKV replication in brain.[30] All brain regions (thalamus, hippocampus, frontal cortex, and cerebellum) examined in the ZIKV-infected mice had significant inflammation, but also abundant apoptotic/necrotic cell damage, which has been described in other ZIKV-infected mouse models.[31] The brains of the ZIKV-infected animals had high levels of ZIKV RNA detected both by RT-PCR and RNAScope. *In vivo*, in ZIKV-infected mice, we detected predominantly ZIKV-infected astrocytes, activated microglia and macrophages, T cells, and neurons by dual ZIKV RNAScope followed by immunohistochemistry. Interestingly, very little to no nestin-1+ neuroprogenitors were infected *in vivo*. Supporting our findings is a recent study describing ZIKV widely infecting the astrocytes and neurons of adult AG129 mice.[32] Spleen, liver, kidney, and lung from all mice were unremarkable without any pathology, and little virus was detected in the spleens of ZIKV animals. Thus, pathology in the ZIKV infection in IFN$^{-/-}$ mice delivered by footpad injection, a physiological route of infection, seems to be highly neurotropic and restricted to brain and not peripheral organs.

In a small animal model of ZIKV disease, we demonstrated that RPV suppressed viral replication, decreased brain inflammation, protected neurons from apoptosis and necrosis, and reversed ZIKV-associated mortality. In the RPV-treated ZIKV-infected animals, there was still significant inflammation in the brain, but no apoptotic/necrotic cell damage was detected, which corresponded to the reversal of mortality. Our findings further indicate that RPV is efficacious at inhibiting ZIKV viral infection in the brain and spleen. Our data would suggest that RPV functions by binding NS5 and, thereby, impacting the enzymatic activity of this viral protein and the productive ZIKV infection cycle.

We recognize that, in the IFN-null context, mice lack all IFN signaling and IFN anti-viral responses, thus succumbing to ZIKV infection with high viral load in brain, with evidence of neurologic disease.[30] However, the fact that RPV can reverse the severe detrimental effects of ZIKV infection in these animals is particularly interesting, and it indicates that direct interaction of RPV with the critically important NS5 viral protein has a negative impact on the *in vivo* propagation of ZIKV in the brain. ZIKV has the inability to cause disease in IFN-competent mice, despite the lethality in the IFN$^{-/-}$ mice. This may be linked to the inability of ZIKV to antagonize mouse IFN responses, unlike in humans. A recent study demonstrated that ZIKV NS5 results in proteasomal degradation of IFN-regulated transcription activator STAT2 in human, but not in mice, possibly explaining the requirement in mice for IFN deficiency.[33] It is possible that the interaction of RPV with NS5 could trigger the proteasomal degradation of STAT2 in the absence of IFN.

Since RPV is a commonly used NNRTI in HIV-infected patients, it would be of interest to see if people with HIV who are treated with RPV are at a lower risk for ZIKV infection. In addition, future studies will include *in vivo* studies utilizing other NNRTIs that were found to be suppressive *in vitro*, including efavirenz and ETR.

MATERIALS AND METHODS

Ethics Statement

All samples were obtained and utilized in accordance with Temple University Human Subjects Protections and the approval of the Institutional Review Board (IRB) and Institutional Animal Care & Use Committee (IACUC).

Computational Evaluation of RPV/NS5 Interaction Sites

Protein Structure Selection, Preparation, and Analysis

We first conducted a survey of available experimental structures of ZIKV NS5, including 20 PDB entries (PDB: 5TMH,[15,17] 5TFR,[18] 5VIM,[34] 5GP1, 5GOZ[35] 5WZ1, 5WZ2, 5WZ3,[16] 5KQR, 5KQS,[36] 5NJU, 5NJV,[37] 5ULP,[38] 5WXB,[39] 5UOB, 5UOC,[40] 5U04,[41] 5M5B,[42] 5M2X, and 6I7P[43]) (https://www.rcsb.org/). All these structures were solved by X-ray diffraction, at resolutions ranging between 1.33 and 3.28 Å. Most of them only comprised one of the two NS5 domains, i.e., MTase and RdRp. We prepared all the collected structures by using the protein preparation Wizard,[44] which included the addition of missing hydrogen atoms, removal of water molecules, and structural integrity check (bond-orders and formal charges) of all protein and ligand atoms. Possible missing side chains were reconstructed using Prime,[45] and protonation states were assigned at pH 7; structure relaxation was performed by restrained minimizations with the OPLS3[46] force field (0.30 Å root-mean-square deviation [RMSD] heavy atom convergence). We then superimposed all NS5 structures onto a common reference template to enable structural comparisons. We finally selected two structures of NS5 (PDB: 5TMH and 5TFR),[17,18] each comprising both domains, for further computational studies. Additionally, we included in our study a number of DENV NS5 structures that were used to refine our computational docking model at the palm site (RdRp domain) (analyzed NS5 DENV structures PDB: 5HMW, 5HMX, 5HMY, 5HMZ, 5HN0, 5I3P, 5JJR, 5I3Q, 5JJS, 5K5M,[22] and 3VWS[23]). All DENV NS5 structures were subject to the outlined protein preparation procedure.

Binding Site Detection

To identify putative sites of NS5 suitable for ligand binding, we used a procedure similar to what we implemented elsewhere.[47] In brief, we

used SiteMap,[19] and sites were detected by applying a standard grid and a more restrictive definition of hydrophobicity. Maps were cropped at 4 Å from the nearest site point.

Ligand Preparation

We prepared a number of ligand structures, including RPV, ETR, and AZT, as well as ligands extracted from co-crystal complexes of NS5 proteins from ZIKV and DENV. All ligands were prepared using the standard LigPrep procedure,[48] with Epik[49] for attributing protonation states and predicting pKa values.

Molecular Docking by Rigid Receptor

We performed molecular docking[50] of RPV and the other ligands against the NS5 protein of ZIKV (PDB: 5TMH).[17] Docking was performed by rigid receptor at the SP level. An exhaustive series of grids was used to define the space for ligand docking. First, we used individual site maps to center the docking space on putative druggable sites detected by SiteMap. Then, for the MTase domain, we used the ligands co-crystallized at the SAM site or the cap site of NS5 (SAH and ^{m7}Gpp; PDB: 5TMH and 5KQS, respectively)[17,36] to define the docking space. Instead, for the RdRp domain, we extracted fragment ligands from DENV NS5[22] that were placed at equivalent locations of ZIKV NS5 (upon superimposition of ZIKV and DENV NS5 structures, followed by relaxation by minimization). These fragment ligands were then used to center the docking grids on the NS5 palm site. For each investigated site, top scoring binding modes of RPV were selected.

Induced-Fit Docking

We selected the most promising binding modes of RILP and ETR at both the SAM site and the palm site for additional refinements by induced-fit docking (IFD).[51] During IFD, docking space was defined by the centroids of rigid-docking ligands, and the SP scoring function was used. To treat the receptor flexibly, all residues within 5 Å of a ligand were refined and optimized using the OPLS3 force field.

Conformational Search

We used ConfGen[25] to perform searches for bioactive conformations of RPV and ETR. During our calculations, we used the OPLS3 force field to perform minimizations; to eliminate redundant conformations, we used a 0.5-Å RMSD cutoff with energy window of 120 kcal/mol.

Computational Prediction of NS5 Mutants

We initially used the structures of NS5 bound to RPV and ETR, as predicted by computational docking, to systematically scan and mutate amino acid residues critical for binding at either the MTase domain (SAM site) or the RdRp domain (palm site). We performed amino acid mutations within the Schrödinger computational suite;[48] upon each mutation, we performed a short minimization to relax the structures around mutant residues and their local structural neighbors. Whenever necessary, we ran a full restrained minimization of the complex to re-optimize the H-bond networks. After excluding that the binding of RPV may occur at the MTase domain (by NS5-MTase truncation followed by site-directed mutagenesis studies and binding affinity predictions; Figure 3A), we visually inspected all mutant complexes at the RdRp domain, and we selected those mutated residues predicted to exert greater effect of RPV binding. Since our initial docking calculations predicted three different binding modes for RPV against the RdRp domain (Figures S7–S10), we prioritized the top most critical residues involved in RPV binding for each docking hypotheses. The final list of residues expected to interact with RPV (and possibly with ETR) included F400, K403, N407, K462, Q463, Y477, R483, D665, D666, R731, E735, R739, T796, and W797. All these residues were mutated to alanine and used to experimentally assess the binding of RPV.

Homology Modeling of NS5 Strains

We used the NS5 protein sequence employed in the experimental work (PRVABC59 strain) to build homology models of NS5. Specifically, PDB: 5TMH (MR766 strain) provided the structural template used in the computational work. Models were generated using the protein structure homology-modeling server SWISS-MODEL.[52] Sequence and structure comparisons of NS5 from the two strains show that all 14 mutant residues, used in this study to infer RPV binding, coincide.

We used software programs distributed by Schrödinger[48] for calculations (protein and ligand preparation, binding site detection, molecular docking, ligand conformational search, and mutational analyses), data visualization, and figure preparation.

Determination of Binding Interactions with DSF

DSF or protein thermal shift assays were completed by use of an Applied Biosystems QuantStudio 6 Flex real time PCR instrument with 384-well plate. In these reactions, the assay plates contained a final volume of 20 μL with PBS (10 mM phosphate and 150 mM NaCl [pH 7.4]) and protein samples (purified ZIKV NS5-MBP or MBP) plus the binding partner (RPV) and protein thermal shift Dye kit (cat# 4461146, diluted 1:125 in kit diluent). The plate was sealed and mixed briefly, followed by plate centrifugation at 1,000 rpm for 2 min. After 30-min incubation at 25°C, the plate was then subjected to thermal shift by ramping the temperature from 25°C to 99°C at 0.05°C increments per second. The relative fluorescence emitted by the thermal shift dye was recorded during the temperature ramp phase and plotted versus temperature. The derivative of these thermal melt curves was determined and Tm calculated from these data. The Tm values were plotted as a function of RPV concentration in GraphPad Prism, and the inflection point of the curve determines the binding affinity of ligand to binding protein. The experiments were completed with n = 4–5 replicate samples per treatment. Each experiment was repeated 3–4 times.

Statistical Analysis

All of the values presented on the graphs are given a mean ± SEM. ANOVA and unpaired Student's t test were used to analyze the statistical significance; p values <0.05 were considered statistically significant.

SUPPLEMENTAL INFORMATION

Supplemental Information can be found online at https://doi.org/10.1016/j.ymthe.2019.10.006.

AUTHOR CONTRIBUTIONS

Conceived the Idea, K.K.; Designed the Experiments, K.K., I.K.S., J.G., T.H.B., H.S.W., J.S., and E.G.; Performed the Experiments, I.K.S., H.S.W., M.D., S.C., A.B., J.A.R., M.H.O., J.S., and E.G.; Interpreted the Data, K.K., I.K.S., J.G., T.H.B., H.S.W., J.S., M.L.K., E.G., and S.A.; Contributed Reagents/Materials/Analysis Tools, K.K., I.K.S., J.G., T.H.B., M.L.K., H.S.W., M.H.O., and S.A.; Wrote the Paper, K.K., I.K.S., J.G., T.H.B., J.S., M.L.K., E.G., and S.A.

CONFLICTS OF INTEREST

The authors declare no competing interests.

ACKNOWLEDGMENTS

The authors wish to thank past and present members of the Department of Neuroscience and Center for Neurovirology, for their support, and sharing of reagents. We greatly appreciate the generosity of Dr. Howard Gendelman for his advice and sharing the results from his laboratory on the detection of RPV in the brains of experimental animals. We express our gratitude to Jessica Otte for her technical assistance and dedications. We would like to also thank Dr. Huaqing Zhao for biostatistical consultation. The computational work was carried out on Temple University's High Performance Computing facility, supported in part by the National Science Foundation through major research instrumentation grant number 1625061 and by the US Army Research Laboratory under contract number W911NF-16-2-0189. This work was supported in part by grants awarded to K.K., and we used services offered by core facilities of the Comprehensive NeuroAIDS Center (CNAC) P30MH092177 awarded to K.K. All data in this manuscript are available from the authors upon reasonable request.

REFERENCES

1. Bogoch, I.I., Brady, O.J., Kraemer, M.U.G., German, M., Creatore, M.I., Kulkarni, M.A., Brownstein, J.S., Mekaru, S.R., Hay, S.I., Groot, E., et al. (2016). Anticipating the international spread of Zika virus from Brazil. Lancet *387*, 335–336.

2. Cao-Lormeau, V.M., Roche, C., Teissier, A., Robin, E., Berry, A.L., Mallet, H.P., Sall, A.A., and Musso, D. (2014). Zika virus, French polynesia, South pacific, 2013. Emerg. Infect. Dis. *20*, 1085–1086.

3. Haddow, A.D., Schuh, A.J., Yasuda, C.Y., Kasper, M.R., Heang, V., Huy, R., Guzman, H., Tesh, R.B., and Weaver, S.C. (2012). Genetic characterization of Zika virus strains: geographic expansion of the Asian lineage. PLoS Negl. Trop. Dis. *6*, e1477.

4. Huang, W.C., Abraham, R., Shim, B.S., Choe, H., and Page, D.T. (2016). Zika virus infection during the period of maximal brain growth causes microcephaly and corticospinal neuron apoptosis in wild type mice. Sci. Rep. *6*, 34793.

5. Musso, D., Roche, C., Robin, E., Nhan, T., Teissier, A., and Cao-Lormeau, V.M. (2015a). Potential sexual transmission of Zika virus. Emerg. Infect. Dis. *21*, 359–361.

6. Musso, D. (2015b). Zika virus transmission from French Polynesia to Brazil. Emerg. Infect. Dis. *21*, 1887.

7. Ventura, C.V., Maia, M., Bravo-Filho, V., Góis, A.L., and Belfort, R., Jr. (2016). Zika virus in Brazil and macular atrophy in a child with microcephaly. Lancet *387*, 228.

8. Besnard, M., Lastere, S., Teissier, A., Cao-Lormeau, V., and Musso, D. (2014). Evidence of perinatal transmission of Zika virus, French Polynesia, December 2013 and February 2014. Euro Surveill. *19*, 20751.

9. Besnard, M., Eyrolle-Guignot, D., Guillemette-Artur, P., Lastère, S., Bost-Bezeaud, F., Marcelis, L., Abadie, V., Garel, C., Moutard, M.L., Jouannic, J.M., et al. (2016). Congenital cerebral malformations and dysfunction in fetuses and newborns following the 2013 to 2014 Zika virus epidemic in French Polynesia. Euro Surveill. *21*, 30181.

10. Culjat, M., Darling, S.E., Nerurkar, V.R., Ching, N., Kumar, M., Min, S.K., Wong, R., Grant, L., and Melish, M.E. (2016). Clinical and Imaging Findings in an Infant With Zika Embryopathy. Clin. Infect. Dis. *63*, 805–811.

11. Calvet, G., Aguiar, R.S., Melo, A.S.O., Sampaio, S.A., de Filippis, I., Fabri, A., Araujo, E.S.M., de Sequeira, P.C., de Mendonça, M.C.L., de Oliveira, L., et al. (2016). Detection and sequencing of Zika virus from amniotic fluid of fetuses with microcephaly in Brazil: a case study. Lancet Infect. Dis. *16*, 653–660.

12. Chimelli, L., Melo, A.S.O., Avvad-Portari, E., Wiley, C.A., Camacho, A.H.S., Lopes, V.S., Machado, H.N., Andrade, C.V., Dock, D.C.A., Moreira, M.E., et al. (2017). The spectrum of neuropathological changes associated with congenital Zika virus infection. Acta Neuropathol. *133*, 983–999.

13. Mlakar, J., Korva, M., Tul, N., Popović, M., Poljšak-Prijatelj, M., Mraz, J., Kolenc, M., Resman Rus, K., Vesnaver Vipotnik, T., Fabjan Vodušek, V., et al. (2016). Zika virus associated with microcephaly. N. Engl. J. Med. *374*, 951–958.

14. Lindenbach, B.D., and Rice, C.M. (2003). Molecular biology of flaviviruses. Adv. Virus Res. *59*, 23–61.

15. Wang, B., Thurmond, S., Hai, R., and Song, J. (2018). Structure and function of Zika virus NS5 protein: perspectives for drug design. Cell. Mol. Life Sci. *75*, 1723–1736.

16. Duan, W., Song, H., Wang, H., Chai, Y., Su, C., Qi, J., Shi, Y., and Gao, G.F. (2017). The crystal structure of Zika virus NS5 reveals conserved drug targets. EMBO J. *36*, 919–933.

17. Wang, B., Tan, X.F., Thurmond, S., Zhang, Z.M., Lin, A., Hai, R., and Song, J. (2017). The structure of Zika virus NS5 reveals a conserved domain conformation. Nat. Commun. *8*, 14763.

18. Upadhyay, A.K., Cyr, M., Longenecker, K., Tripathi, R., Sun, C., and Kempf, D.J. (2017). Crystal structure of full-length Zika virus NS5 protein reveals a conformation similar to Japanese encephalitis virus NS5. Acta Crystallogr. F Struct. Biol. Commun. *73*, 116–122.

19. Halgren, T. (2007). New method for fast and accurate binding-site identification and analysis. Chem. Biol. Drug Des. *69*, 146–148.

20. Das, K., Bauman, J.D., Clark, A.D., Jr., Frenkel, Y.V., Lewi, P.J., Shatkin, A.J., Hughes, S.H., and Arnold, E. (2008). High-resolution structures of HIV-1 reverse transcriptase/TMC278 complexes: strategic flexibility explains potency against resistance mutations. Proc. Natl. Acad. Sci. USA *105*, 1466–1471.

21. Lansdon, E.B., Brendza, K.M., Hung, M., Wang, R., Mukund, S., Jin, D., Birkus, G., Kutty, N., and Liu, X. (2010). Crystal structures of HIV-1 reverse transcriptase with etravirine (TMC125) and rilpivirine (TMC278): implications for drug design. J. Med. Chem. *53*, 4295–4299.

22. Lim, S.P., Noble, C.G., Seh, C.C., Soh, T.S., El Sahili, A., Chan, G.K., Lescar, J., Arora, R., Benson, T., Nilar, S., et al. (2016). Potent allosteric Dengue virus NS5 polymerase inhibitors: mechanism of action and resistance profiling. PLoS Pathog. *12*, e1005737.

23. Noble, C.G., Lim, S.P., Chen, Y.L., Liew, C.W., Yap, L., Lescar, J., and Shi, P.Y. (2013). Conformational flexibility of the Dengue virus RNA-dependent RNA polymerase revealed by a complex with an inhibitor. J. Virol. *87*, 5291–5295.

24. Noble, C.G., Lim, S.P., Arora, R., Yokokawa, F., Nilar, S., Seh, C.C., Wright, S.K., Benson, T.E., Smith, P.W., and Shi, P.Y. (2016). A conserved pocket in the Dengue virus polymerase identified through fragment-based screening. J. Biol. Chem. *291*, 8541–8548.

25. Watts, K.S., Dalal, P., Murphy, R.B., Sherman, W., Friesner, R.A., and Shelley, J.C. (2010). ConfGen: a conformational search method for efficient generation of bioactive conformers. J. Chem. Inf. Model. *50*, 534–546.

26. Ericsson, U.B., Hallberg, B.M., Detitta, G.T., Dekker, N., and Nordlund, P. (2006). Thermofluor-based high-throughput stability optimization of proteins for structural studies. Anal. Biochem. *357*, 289–298.

27. Niesen, F.H., Berglund, H., and Vedadi, M. (2007). The use of differential scanning fluorimetry to detect ligand interactions that promote protein stability. Nat. Protoc. *2*, 2212–2221.

28. Pantoliano, M.W., Petrella, E.C., Kwasnoski, J.D., Lobanov, V.S., Myslik, J., Graf, E., Carver, T., Asel, E., Springer, B.A., Lane, P., and Salemme, F.R. (2001). High-density miniaturized thermal shift assays as a general strategy for drug discovery. J. Biomol. Screen. *6*, 429–440.

29. Thammaporn, R., Ishii, K., Yagi-Utsumi, M., Uchiyama, S., Hannongbua, S., and Kato, K. (2016). Mass spectrometric characterization of HIV-1 reverse transcriptase interactions with non-nucleoside reverse transcriptase inhibitors. Biol. Pharm. Bull. *39*, 450–454.

30. Lazear, H.M., Govero, J., Smith, A.M., Platt, D.J., Fernandez, E., Miner, J.J., and Diamond, M.S. (2016). A mouse model of Zika virus pathogenesis. Cell Host Microbe *19*, 720–730.

31. Dowall, S.D., Graham, V.A., Rayner, E., Atkinson, B., Hall, G., Watson, R.J., Bosworth, A., Bonney, L.C., Kitchen, S., and Hewson, R. (2016). A susceptible mouse model for Zika virus infection. PLoS Negl. Trop. Dis. *10*, e0004658.

32. Zukor, K., Wang, H., Siddharthan, V., Julander, J.G., and Morrey, J.D. (2018). Zika virus-induced acute myelitis and motor deficits in adult interferon αβ/γ receptor knockout mice. J. Neurovirol. *24*, 273–290.

33. Grant, A., Ponia, S.S., Tripathi, S., Balasubramaniam, V., Miorin, L., Sourisseau, M., Schwarz, M.C., Sánchez-Seco, M.P., Evans, M.J., Best, S.M., and García-Sastre, A. (2016). Zika virus targets human STAT2 to inhibit type 1 interferon signaling. Cell Host Microbe *19*, 882–890.

34. Bukrejewska, M., Derewenda, U., Radwanska, M., Engel, D.A., and Derewenda, Z.S. (2017). Crystal structures of the methyltransferase and helicase from the ZIKA 1947 MR766 Uganda strain. Acta Crystallogr. D Struct. Biol. *73*, 767–774.

35. Zhang, C., Feng, T., Cheng, J., Li, Y., Yin, X., Zeng, W., Jin, X., Li, Y., Guo, F., and Jin, T. (2017). Structure of the NS5 methyltransferase from Zika virus and implications in inhibitor design. Biochem. Biophys. Res. Commun. *492*, 624–630.

36. Coloma, J., Jain, R., Rajashankar, K.R., García-Sastre, A., and Aggarwal, A.K. (2016). Structures of NS5 methyltransferase from Zika virus. Cell Rep. *16*, 3097–3102.

37. Chatrin, C., Talapatra, S.K., Canard, B., and Kozielski, F. (2017). The structure of the binary methyltransferase-SAH complex from Zika virus reveals a novel conformation for the mechanism of mRNA capping. Oncotarget *9*, 3160–3171.

38. Jain, R., Butler, K.V., Coloma, J., Jin, J., and Aggarwal, A.K. (2017). Development of a S-adenosylmethionine analog that intrudes the RNA-cap binding site of Zika methyltransferase. Sci. Rep. *7*, 1632.

39. Zhou, H., Wang, F., Wang, H., Chen, C., Zhang, T., Han, X., Wang, D., Chen, C., Wu, C., Xie, W., et al. (2017). The conformational changes of Zika virus methyltransferase upon converting SAM to SAH. Oncotarget *8*, 14830–14834.

40. Zhao, B., Yi, G., Du, F., Chuang, Y.C., Vaughan, R.C., Sankaran, B., Kao, C.C., and Li, P. (2017). Structure and function of the Zika virus full-length NS5 protein. Nat. Commun. *8*, 14762.

41. Godoy, A.S., Lima, G.M., Oliveira, K.I., Torres, N.U., Maluf, F.V., Guido, R.V., and Oliva, G. (2017). Crystal structure of Zika virus NS5 RNA-dependent RNA polymerase. Nat. Commun. *8*, 14764.

42. Coutard, B., Barral, K., Lichière, J., Selisko, B., Martin, B., Aouadi, W., Lombardia, M.O., Debart, F., Vasseur, J.J., Guillemot, J.C., et al. (2017). Zika virus methyltransferase: structure and functions for drug design perspectives. J. Virol. *91*, e02202–e02216.

43. Ferrero, D.S., Ruiz-Arroyo, V.M., Soler, N., Usón, I., Guarné, A., and Verdaguer, N. (2019). Supramolecular arrangement of the full-length Zika virus NS5. PLoS Pathog. *15*, e1007656.

44. Sastry, G.M., Adzhigirey, M., Day, T., Annabhimoju, R., and Sherman, W. (2013). Protein and ligand preparation: parameters, protocols, and influence on virtual screening enrichments. J. Comput. Aided Mol. Des. *27*, 221–234.

45. Jacobson, M.P., Pincus, D.L., Rapp, C.S., Day, T.J., Honig, B., Shaw, D.E., and Friesner, R.A. (2004). A hierarchical approach to all-atom protein loop prediction. Proteins *55*, 351–367.

46. Harder, E., Damm, W., Maple, J., Wu, C., Reboul, M., Xiang, J.Y., Wang, L., Lupyan, D., Dahlgren, M.K., Knight, J.L., et al. (2016). OPLS3: a force field providing broad coverage of drug-like small molecules and proteins. J. Chem. Theory Comput. *12*, 281–296.

47. Gianti, E., Messick, T.E., Lieberman, P.M., and Zauhar, R.J. (2016). Computational analysis of EBNA1 "druggability" suggests novel insights for Epstein-Barr virus inhibitor design. J. Comput. Aided Mol. Des. *30*, 285–303.

48. Schrödinger Release (2018). 2018-2: LigPrep (New York, NY: Schrödinger, LLC).

49. Shelley, J.C., Cholleti, A., Frye, L.L., Greenwood, J.R., Timlin, M.R., and Uchimaya, M. (2007). Epik: a software program for pK(a) prediction and protonation state generation for drug-like molecules. J. Comput. Aided Mol. Des. *21*, 681–691.

50. Friesner, R.A., Banks, J.L., Murphy, R.B., Halgren, T.A., Klicic, J.J., Mainz, D.T., Repasky, M.P., Knoll, E.H., Shelley, M., Perry, J.K., et al. (2004). Glide: a new approach for rapid, accurate docking and scoring. 1. Method and assessment of docking accuracy. J. Med. Chem. *47*, 1739–1749.

51. Sherman, W., Beard, H.S., and Farid, R. (2006). Use of an induced fit receptor structure in virtual screening. Chem. Biol. Drug Des. *67*, 83–84.

52. Waterhouse, A., Bertoni, M., Bienert, S., Studer, G., Tauriello, G., Gumienny, R., Heer, F.T., de Beer, T.A.P., Rempfer, C., Bordoli, L., et al. (2018). SWISS-MODEL: homology modelling of protein structures and complexes. Nucleic Acids Res. *46* (W1), W296–W303.

YMTHE, Volume *27*

Supplemental Information

Suppression of Zika Virus Infection in the Brain by the Antiretroviral Drug Rilpivirine

Ilker Kudret Sariyer, Jennifer Gordon, Tricia H. Burdo, Hassen S. Wollebo, Eleonora Gianti, Martina Donadoni, Anna Bellizzi, Stephanie Cicalese, Regina Loomis, Jake A. Robinson, Vincenzo Carnevale, Joseph Steiner, Mehmet H. Ozdener, Andrew D. Miller, Shohreh Amini, Michael L. Klein, and Kamel Khalili

MATERIALS AND METHODS

Cell lines and culture. Primary human fetal astrocytes (PHFA), neurons (PHFN), and microglia (PHFM) were obtained from Comprehensive NeuroAIDS Center (CNAC) tissue culture core at Temple University Lewis Katz Medical School. hNPCs (H9-derived) were purchased from Gibco and maintained in neurobasal medium supplemented with 1% B-27, 1% glutamax, and 1% gentamycin. Astrocytes were maintained in DMEM/F12 (Gibco, Thermofisher Scientific), containing 15% FBS, 0.1% Gentamycin, and 0.1% insulin from bovine (Sigma). Microglia were maintained in DMEM/F12 (Gibco, Thermofisher Scientific), containing 10% FBS, 0.1% Gentamycin, D-Biotin (0.1 µg/ml), and 0.1% insulin from bovine (Sigma). Neurons were seeded into poly-D-lysine coated plates and kept in neurobasal medium containing1% glutamax, 1% B-27 supplement, 0.1% gentamycin, and 0.1% amphotericin B. Half of the neuronal growth medium was replaced with fresh medium every 3 to 4 days.

ZIKV strains and propagation. ZIKV strain PRVABC59 is isolated from a patient isolate in Puerto Rico in 2015, that was obtained from ATCC (VR-1843) and propagated in Vero cells for further production and purification. Culture supernatants from Vero cells infected with ZIKV were collected at 4 dpi and centrifuged at 3,000 RPM for 15 minutes to remove cell debris. ZIKV particles were concentrated by ultracentrifugation of the clarified media for 4 hours at 23,600 RPM at 4 °C. Media was aspirated, and viral particles re-suspended in 1 mL PBS. Virus was further purified utilizing an Optiprep discontinuous 20/55% gradient and ultracentrifugation. Optiprep, a 60% iodixanol solution was diluted into a 20% and 55% layer, 16 mL each, with 20% layered on top of the 55% solution. Viral particles were harvested from the gradient interface and kept frozen at -80 °C or used for plaque-forming assay for infectivity quantification.

Plaque-forming assay. Vero cells were seeded in 6 well plates at a concentration of 1 X 10^6 cells/well 48 hours prior to inoculation and grown in DMEM containing 5% FBS and 1% penicillin/streptomycin. On day of infection, serial dilutions of ZIKV infected culture medium were made by diluting 100 uL media in 900 uL OptiMEM from 10^{-2} to 10^{-6} dilutions. 900 uL of each viral

dilution was added to confluent vero cells and inoculated at 37 °C for 2 hours. Inoculum was aspirated and fresh DMEM was added and changed every two days. On day five post-infection, vero cells were fixed in 10%

formaldehyde in PBS and stained with a 0.1% solution of crystal violet in 70% methanol, and the virus titers were calculated by scoring the plaque-forming units (PFU).

ZIKV infection in primary human CNS cells. To investigate ZIKV propagation in the CNS cells, PHFA, PHFM, PHFN, PHAA, and hNPCs (H9) cells were seeded into 6-well plates and infected with ZIKV (0.1 PFU). Cells were seeded at a density of 1 x 10^6, grown to confluency and inoculated with 1 mL OptiMEM containing diluted virus. Cells were incubated for 2 hours at 37 °C, before media was exchanged for fresh media. Media was collected from infected cells at various time points of post-infections, centrifuged at 3,000 RPM for 15 minutes to remove cell debris, and used in real time qRT-PCR for analysis of shed viral particles. Whole cell lysates and RNA samples were also collected from the cells. Protein lysates were collected by lysing cells in 1X TNN buffer with protease inhibitor cocktail (Sigma), rotating for 30 minutes, followed by centrifugation to collect supernatant. RNA was purified via Trizol Reagent protocol (Invitrogen, Thermofisher Scientific). Whole cell lysates were used for Western blot analysis of viral proteins. Cell RNA was either analyzed for viral RNA copies via real time qRT-PCR or by RT-PCR for viral genes.

Real time qRT-PCR. Either 10 uL media from infected cells or 20 ng cell RNA or tissue RNA was used for real time qRT-PCR analysis of ZIKV copies as described by Lanciotti et al.[1]. All real-time assays were performed by using the QuantiTect Probe RT-PCR kit (QIAGEN, Valencia, CA, USA) with amplifications in the LightCycler 96 instrument (Roche, Indianapolis, IN, USA). The standard curve was generated using a ZIKV with known copies (3.2 x 10^7 viral copies/mL) and diluted 10 folds. Ct values for each sample were converted to viral copies/ml using the following equation:

$$Quantity = 10^{\frac{Ct-b}{m}}$$

Where quantity is ZIKV copies/ml, Ct is the threshold cycle at which the fluorescence value for the sample was significantly higher than background, b is the y intercept of the standard curve, and m is the slope of the standard curve. The following ZIKV specific primers were used in the reactions:

ZIKV-1086 (1086–1102) CCGCTGCCCAACACAAG,

ZIKV-1162c (1162–1139) CCACTAACGTTCTTTTGCAGACAT,

ZIKV-1107-FAM (1107–1137) AGCCTACCTTGACAAGCAGTCAGACACTCAA-6FAM.

Western blot analysis. Whole-cell extracts (WCE) were prepared from cells after washing with PBS by lysingwith TNN lysis buffer (40 mM Tris-HCL pH 7.4, 150 mM NaCl, 1 mM DTT, 1 mM EDTA, 1% NP40, and 1% protease inhibitors cocktail). Protein extracts were eluted with Laemmli sample buffer, heated at 95 °C for 10 min, resolved by SDS—PAGE and transferred to reinforced supported nitrocellulose membranes (Whatman, Germany) for 2 h at 4 °C in a transfer buffer containing 25 mM Tris (pH 7.4), 200 mM glycine, and 20% methanol. Membranes were blocked for 1 h at room temperature with 10% nonfat dry milk in PBS with 0.1% Tween-20 (PBST), washed and incubated with primary antibodies overnight in 5% nonfat dry milk at 4 °C. The blots were subsequently washed three times and incubated with IRDye 800CW goat anti-mouse and IRDye 680RD goat anti-rabbit secondary antibodies and visualized with an Odyssey CLx Imaging System (LI-COR, Inc.,). The following antibodies were used for Western blot: Zika Capsid antibody (GeneTex, cat#GTX133304), β Actin, and GAPDH.

MTT cell viability assay

Primary human fetal astrocytes were cultured in 12-well tissue culture plates and treated in triplicate with different concentrations of RPV (0, 1, 5, 10, 25, and 50 uM) based on previous studies in culture conditions[4,5] for 48 hours. After treatments, cells were incubated for 2 hours at 37°C with 150 µl of MTT (3-(4 5-dimethylthiazol-2-yl)-2 5-diphenyltetrazolium bromide) at 0.5 mg/ml working solution. The converted insoluble purple formazan was solubilized with 500 µl of

acidic isopropanol (0.004 M HCl in isopropanol). Absorbance of the converted formazan was measured at a wavelength of 570 nm with a background subtraction at 650 nm.

NNRTIs treatment of primary human CNS cells for ZIKV replication inhibition. The following HIV non-nucleoside reverse transcriptase inhibitors (NNRTIs) were tested in PHFA: Rilpivirine (ApexBio Tech LLC cat# A3765), Efavirenz (Sigma, cat# SML0536), Etravirine (ApexBio Tech LLC, cat# B2224), Delaviridine mesylate (DM) (Sigma, cat#PZ0180), Nevirapine (Nevi) (Selleckchem, cat#S1742). As a control, 3'-Azido-3'-deoxythymidine (AZT) (Sigma, cat# A2169) was used. These inhibitors were solubilized in DMSO to concentrations of 5 and 10 µg/mL, and added to PHFA seeded into 100 mm dishes at a concentration of 1.5 x 10^6 cells/dish. PHFA were inoculated with ZIKV at 0.5 pfu and treated once daily with the NNRTIs for 1 to 4 DPI, followed by whole cell lysate and RNA collection.

Immunocytochemistry. PHFA cells were seeded in two-well chamber slides, infected with ZIKV (0.1 PFU), and treated once daily with the RPV or AZT for 1 to 4 DPI. Cells were fixed with cold 4% paraformaldehyde for 20 minutes and washed three times with PBS. Cells were treated with a 5% BSA solution, followed by incubation with anti-GFAP (mouse) and anti-NS1 (rabbit) antibodies. Cells were then incubated with rhodamine and FITC-conjugated secondary antibodies, mounted with aqueous mounting medium with DAPI, and examined under immunoflourescence microscope.

Recombinant NS5 RNA polymerase preparation. Preparation of NS5 RNA polymerase was carried out with a modification of a protocol previously described[2]. The ZIKV NS5 was cloned into the pMAL™-c5X vector at the SalI and HindIII sites. MBP-NS5 expression was induced for 4 hours at 28 °C by adding isopropyl β-D-1-thiogalactopyranoside (IPTG), 0.5 mM final concentration, to *E. coli*. The cells were then harvested by centrifugation and re-suspended in 20 mM Tris-HCl pH 7.4 with 200 mM NaCl and 1 mM EDTA (amylose fast flow column buffer). Re-suspended cells were incubated on ice with lysozyme and protease inhibitor cocktail and then lysed by sonication. Clear lysates, obtained after centrifugation, were incubated overnight at 4 °C

with Amylose Resin High Flow beads (NEB). MBP-NS5 protein was then washed four times with amylose fast flow column buffer and processed to Factor Xa cleavage. MBP-NS5 fusion protein was incubated for 5 hours at room temperature in the presence of 2 mM $CaCl_2$ and Factor Xa. After centrifugation, supernatant was collected and used for NS5 activity assay. MT domain (from amino acid 1 to amino acid 264) was cloned into pMAL™-c5X vector at the SalI and BamHI sites. RdRp domain (from amino acid 265 to amino acid 903) was cloned into pMAL™-c5X vector at the EcoRI and HindIII sites. RdRp-14A was generated by substituting the corresponding amino acid residues with into alanine. RdRp-14A mutant was cloned into pMAL™-c5X vector at the EcoRI and HindIII sites using a gBlock fragment.

List of primers: NS5-full-length, F: AAGATTGTCGACGGAGGTGGGACGGGAGAGACT R: AAGATTAAGCTTTCACAACACTCCGGGTGTGGA, NS5-MTase-domain: F: AAGATTGTCGACGGAGGTGGGACGGGAGAGACT, R: AAGATTGGATCCTCATCGTGTACCCGAGCCGAG, NS5-RdRp-domain, F: AAGATTGAATTCGCTGTGGCAAGCTGTGCTG, R: AAGATTAAGCTTTCACAACACTCCGGGTGTGGA. The RdRp-14A mutant was also cloned into a mammalian expression vector (pCDNA6-myc-his-A) at HindIII-XhoI restriction enzyme sites by utilizing following primers: F: AAGATTAAGCTTATGGCTGTGGCAAGCTGTG, R: AAGATTCTCGAGCAACACTCCGGGTGTGGA.

NS5 RNA polymerase activity assay. The viral RNA polymerase NS5 ability to synthesize new viral RNA was analyzed using an *in vitro* activity assay, based on a previously described protocol[3]. One µg of ZIKV RNA and 500 ng of NS5 full-length or mutant protein (14A) with side directed mutagenesis were added to a reaction buffer containing 50 mM HEPES (pH 7.3), 0.4 mM dithiothreitol (DTT), 3 mM $MgCl_2$ and 0.4 mM of ATP, GTP, CTP and biotinylated- UTP ribonucleotides. The ribonucleotide UTP was labeled in an equimolar ratio of biotinylated-UTP and digoxigenin-UTP (DIG-UTP), for quantification of newly replicated RNA. The reaction mixtures were incubated for 1 h at 30 °C in the presence or absence of rilpivirine and

azidothymidine. The reactions were then stopped with addition of EDTA at a final concentration of 10 mM. In order to detect the incorporation of labelled UTP nucleotides, an Alpha Technology amplified luminescent proximity homogeneous assay was performed. Anti-DIG-acceptor and streptavidin-donor beads, at working concentration of 20 µg/mL, were incubated with the reaction mixture for 2 hours at room temperature in a white 96-well plate. Then, the amounts of beads bound to the DIG-labeled UTP of newly synthesized RNA could be detected by reading the plates in ALPHA compatible plate reader (Tecan). Reaction mixture without NS5 or with MBP alone was used as controls.

Mouse ZIKV infection and rilpivirine treatment. Nine IFNR knockout transgenic ($IFNR^{-/-}$) mice, obtained from Jackson laboratories, at four months were divided into three groups in two different set of experiments; 1. RPV treatment and mock infection (n=3 or n=6), 2. ZIKV infection, no treatment (n=3 or n=6), and 3. RPV treatment and ZIKV infection (n=3 or n=6). Six or twelve animals were started treatment with RPV (12.5 µg per 25 g mouse via intraperitoneal (IP) injections) two days prior ZIKV or mock infection. RPV treatments were continued daily until necropsy. Six in the first set and 12 in the second cohort of mice were infected with PRVABC59 strain of ZIKV (10^3 pfu in 20ul PBS) and three or six with a mock infection (PBS only) through footpad injections.

Mouse clinical scores and necropsy. All mice were monitored daily for survival and signs of disease as well as twice-daily weight checks and grasp test analysis. Daily physical, behavior, and motor coordination/paralysis inspections were also performed. Clinical scores were determined by grasp test and physical-behavior assessments. Mice were sacrificed based on weight loss, physical, behavior, and motor function deficits. All mice were sacrificed at the endpoint of the study at day 14 post infection. Brains were removed and half were harvested, homogenized for total RNA isolation using a commercially available kit (RNeasy mini, Qiagen). RNA samples from ZIKV-infected animals were stored at -80 °C until virus titration. The other half

of the brains were fixed in 10% neutral buffered formalin and paraffin embedded for histological examination. Organs (spleen, liver, kidney and lung) were also removed, fixed in formalin and processed for histological examination.

Histopathological Evaluation of Brain and Organ Pathology. Tissues were sectioned in a sagittal orientation at 5um for histological analysis. Slides were deparaffinized through xylene, rehydrated in graded ethanols, and stained with hematoxylin and eosin. Slides were evaluated blindly for histopathological changes (neuronal loss, gliosis, and inflammation) by a board certified veterinary anatomical pathologist (A.D.M.).

RNAscope in situ hybridization and quantitation. Zika viral RNA in the brain (frontal cortex, hippocampus, thalamus and cerebellum) and organs (spleen, liver, kidney and lung) was visualized using RNAscope in situ hybridization, according to specifications of the manufacturer (ACD Bio). Slides were deparaffinized through xylene, washed in 100% ethanol, and air-dried. Sections were treated with heat-induced target retrieval (92-100 °C) and incubated with protease (40°C). The probe was designed to target Zika viral RNA at the 866-1763 region, based off MR766 sequence (ACD Bio). The probe was hybridized in a humidity chamber at 40 °C for 2 hours. The Zika viral RNA was detected by amplification and chromogenic development using the alkaline phosphatase (AP), red chromogen detection kit (ACD Bio). Sections were counterstained with hematoxylin, dried at 60 °C and mounted. Slides were blindly imaged for quantitation of viral signal. Viral RNA was detected using Texas-Red filter fluorescence (10, 400x non-overlapping images) with a Keyence BZ-X700 Microscope. Zika viral RNA area was quantified using batch fluorescent analysis and reported as the average positive area. Zika-infected (ZIKV) Zika-infected + RPV-treated (ZIKV + RPV) groups were compared by unpaired, non-parametric t-test (Mann-Whitney), with a significance of $p<0.05$.

Dual RNAscope and immunohistochemistry. Sections were deparaffinized, rehydrated, and heat-treated with sodium citrate antigen retrieval (92-100 °C). No protease was applied to

sections. Sections were blocked with 5% levamisole in PBS for 10 minutes to block endogenous AP. Sections were hybridized with the Zika RNA probe and amplified with the AP, red chromogen kit, according to the manufacturer (ACDBio). Following verification of RNAscope detection, slides were blocked with dual endogenous enzyme block (Dako) and 10% fetal bovine serum in PBS. Sections were incubated overnight at 4 °C with antibodies against astrocytic GFAP (1:2000, ProteinTech), microglia-macrophage marker Iba1 (1:600, Wako Chemicals), T-lymphocyte marker CD3 (1:300 Dako), neuronal marker NeuN (1:500, ProteinTech), and nestin (1:300; BD Biosciences). Slides were visualized using a horseradish peroxidase (HRP)-conjugated secondary antibody and 3,3'-Diaminobenzidine chromogen (DAB)(Dako), with hematoxylin counterstain. Sections were dried at 60°C, dipped in xylene and mounted. Slides were imaged in bright-field at 200x and 600x magnification, using a Keyence BZ-X700 Microscope and accompanying software for analysis.

Statistical Analysis. All of the values presented on the graphs are given a mean ± SEM. Analysis of variance and unpaiared Student's t-test were used to analyze the statistical significance. p-values of <0.05 were considered statistically significant.

References

1. Lanciotti, R.S., et al. Genetic and serologic properties of Zika virus associated with an epidemic, Yap State, Micronesia, 2007. *Emerg. Infect. Dis.* **14**, 1232-1239 (2008).
2. Saribas, A.S., Arachea, B.T., White, M.K., Viola, R.E., Safak, M. Human polyomavirus JC small regulatory agnoprotein forms highly stable dimers and oligomers: implications for their roles in agnoprotein function.*Virology* **420,** 51-65 (2011).
3. Sacramento, C.Q, et al. The clinically approved antiviral drug sofosbuvir inhibits Zika virus replication. *Sci. Rep*. **7**, 40920 (2017).

4. Julieta Díaz-Delfín, Pere Domingo, Maria Gracia Mateo, Maria del Mar Gutierrez, Joan Carles Domingo, Marta Giralt, Francesc Villarroya. Effects of Rilpivirine on Human Adipocyte Differentiation, Gene Expression, and Release of Adipokines and Cytokines. Antimicrob Agents Chemother. 2012 Jun; 56(6): 3369–3375.

5. Barry C Johnson, Gary T Pauly, Ganesha Rai, Disha Patel, Joseph D Bauman, Heather L Baker, Kalyan Das, Joel P Schneider, David J Maloney, Eddy Arnold, Craig J Thomas, Stephen H Hughes. A comparison of the ability of rilpivirine (TMC278) and selected analogues to inhibit clinically relevant HIV-1 reverse transcriptase mutants. Retrovirology. 2012; 9: 99.

Supplemental Figures and Figure Legends

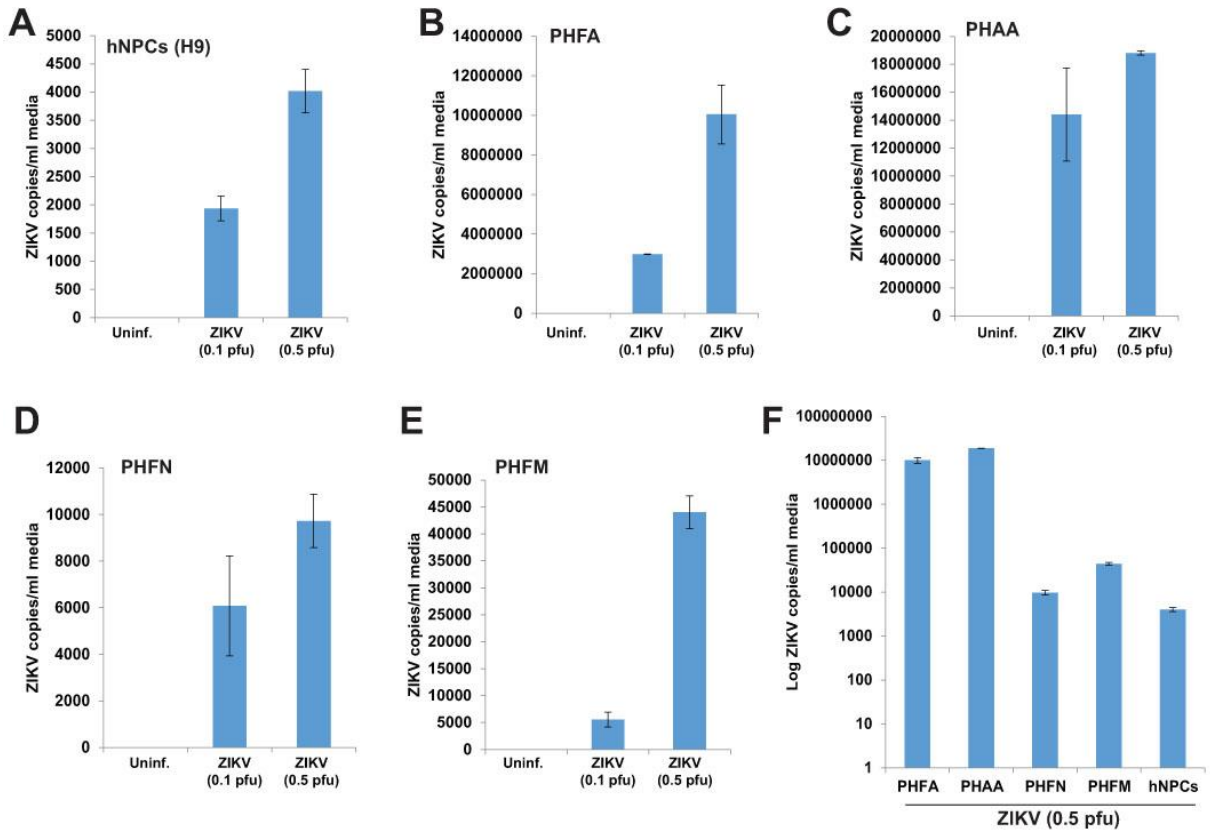

Supplemental Figure 1: ZIKV infection in primary cultures of brain cells. A. Human neuronal progenitors (NPCs-H9), **B.** Primary human fetal astrocytes (PHFA), **C.** Primary human adult astrocytes (PHAA), **D.** primary human fetal neurons (PHFN), and **E.** primary human fetal microglial cells (PHFM), were infected with 0.1 and 0.5 pfu ZIKV, and culture supernatants were analyzed by real time Q-RT-PCR at three days post-infections. ZIKV RNA copies per ml culture media were displayed as bar graphs. **F.** Log ZIKV viral loads in culture media from each cell type infected with 0.5 pfu ZIKV were displayed as bar graph.

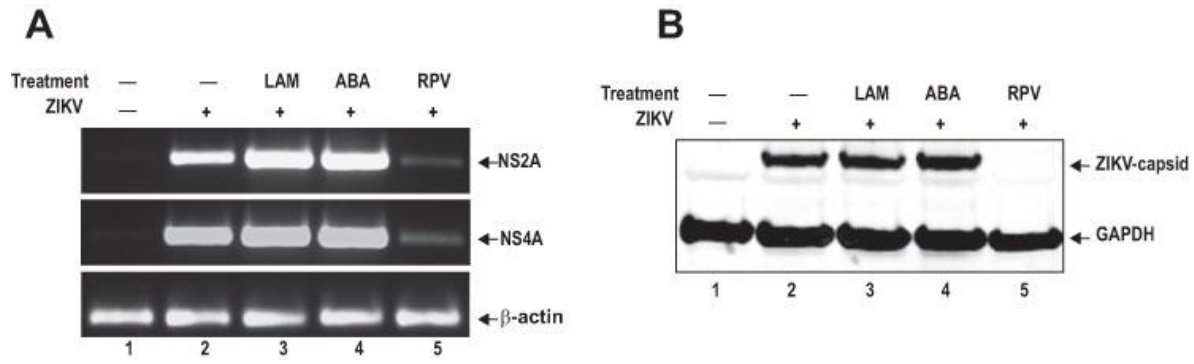

Supplemental figure 2: Effects of NNRTI on ZIKV replication in PHFA. PHFAs were infected with PRVABC59 strain of ZIKV (0.5 pfu). Cells were treated daily with LAM, ABA, and RPV (10 µg/ml). At 3 dpi, RNA lysates from cellular pellets and whole cell protein lysates were collected for analysis. A. The encoding sequence of ZIKV NS1, NS2A, and NS4A were amplified by RT-PCR in total RNA samples obtained from ZIKV infected cells, separated on a DNA agarose gel, and amplification products were visualized by ethidium bromide staining. Actin was also amplified and analyzed from the same set of samples and shown as control. B. Whole cells protein lysates from the same set of infection studies presented in panel A were processed by western blotting for the detection of ZIKV capsid protein expression by a specific antibody. GAPDH was also probed in the same membranes after stripping off the first antibody complex, and used as loading control.

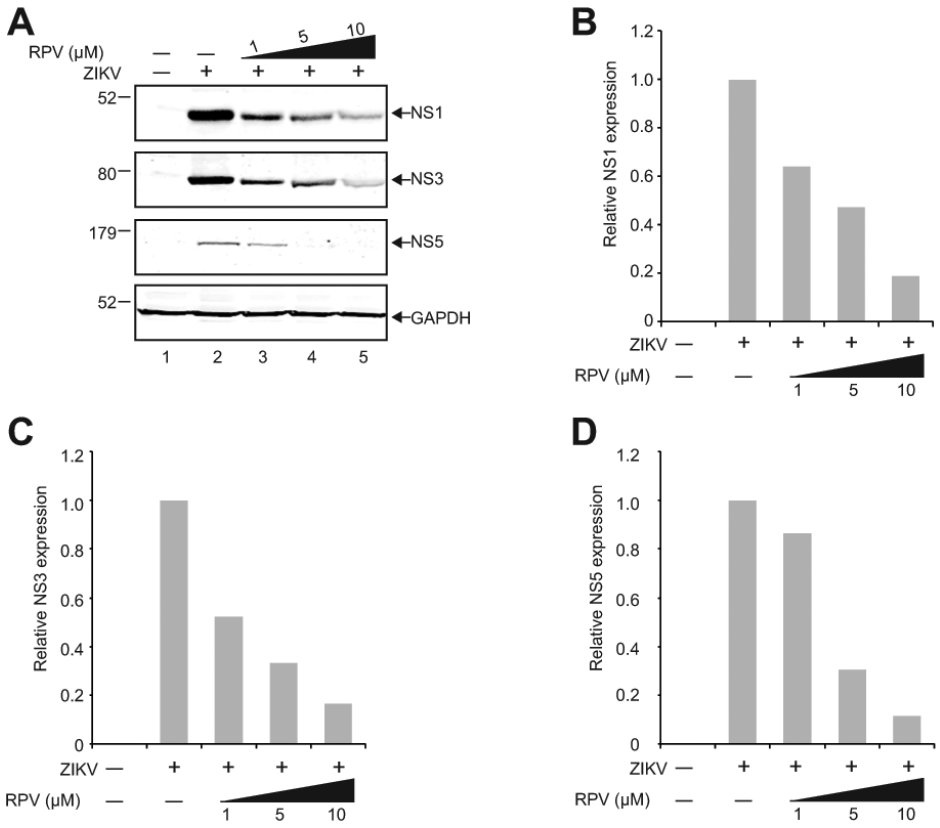

Supplemental Figure 3: Inhibition of ZIKV infection of PHFA by RPV. A. PHFA were infected with PRVABC59 strain of ZIKV (0.5 pfu) and treated with increasing concentrations of RPV (1, 5, and 10 μg/ml). Whole cell protein lysates were prepared at 4 dpi and processed by Western blotting for the detection of NS1, NS3, and NS5 protein expression. GAPDH was also probed in the same membranes after stripping off the first antibody complex, and used as loading control. **B-D.** The band intensities of NS1 (**B**), NS3 (**C**), and NS5 (**D**) shown in panel A were determined, normalized to GAPDH, and shown as bar graph as relative protein expression under each condition.

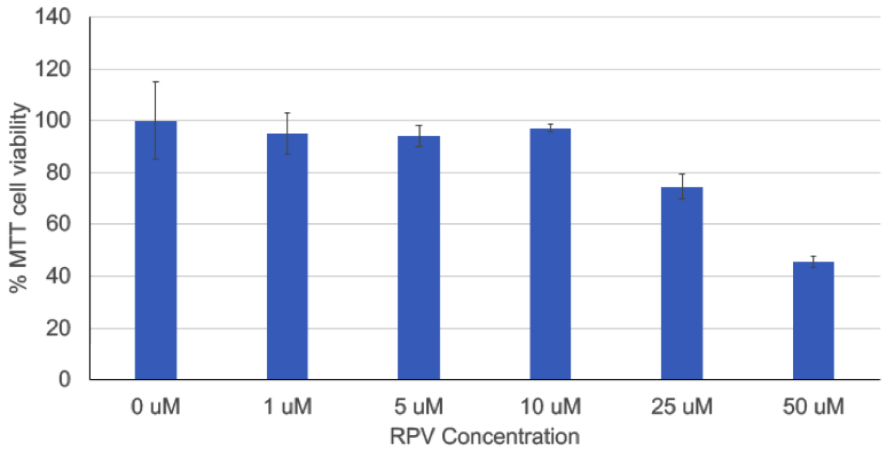

Supplemental Figure 4: Effect of RPV on viability of primary human fetal astrocytes (PHFA). PHFA cells were plated in 12 well culture dishes. Cells were treated with RPV at 0, 1, 5, 10, 25, and 50 uM concentrations. Cellular viability was assessed at 48 hr post treatments by MTT (3-(4 5-dimethylthiazol-2-yl)-2 5-diphenyltetrazolium bromide) assay. Data are mean + SEM of three independent replicates.

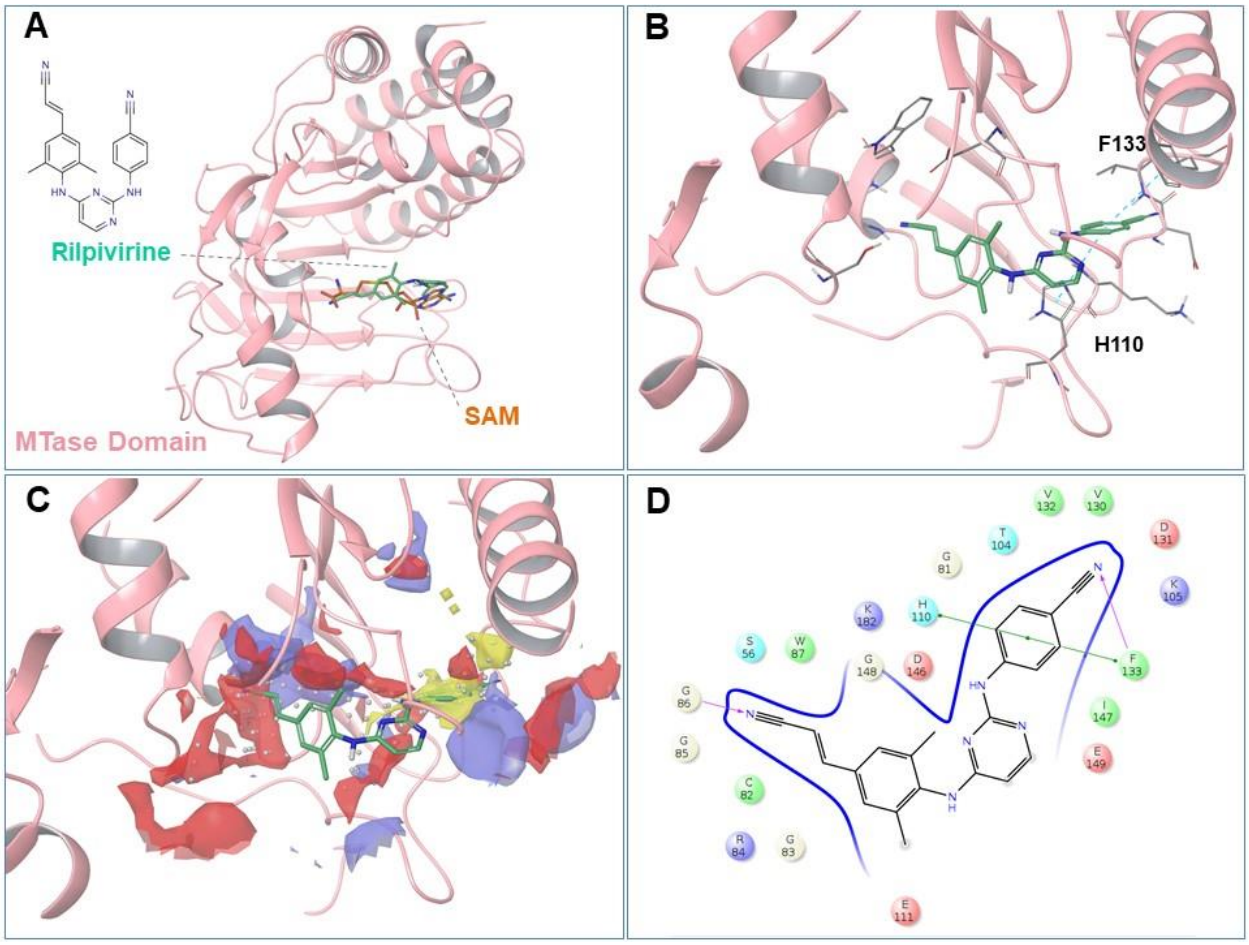

Supplemental Figure 5: Putative binding mode of RPV at the SAM site (Mtase domain). The structure of ZIKV NS5 is shown in New Cartoon representation, in pink color. A. Docking mode of RPV (green carbons) superimpose well with the crystallographic pose of the methyl donor SAH (orange carbons). B-D. Critical binding interactions are shown. In C, RPV is superimposed to complementary site map features (yellow: hydrophobic, red and blue: ligand acceptor and donor maps).

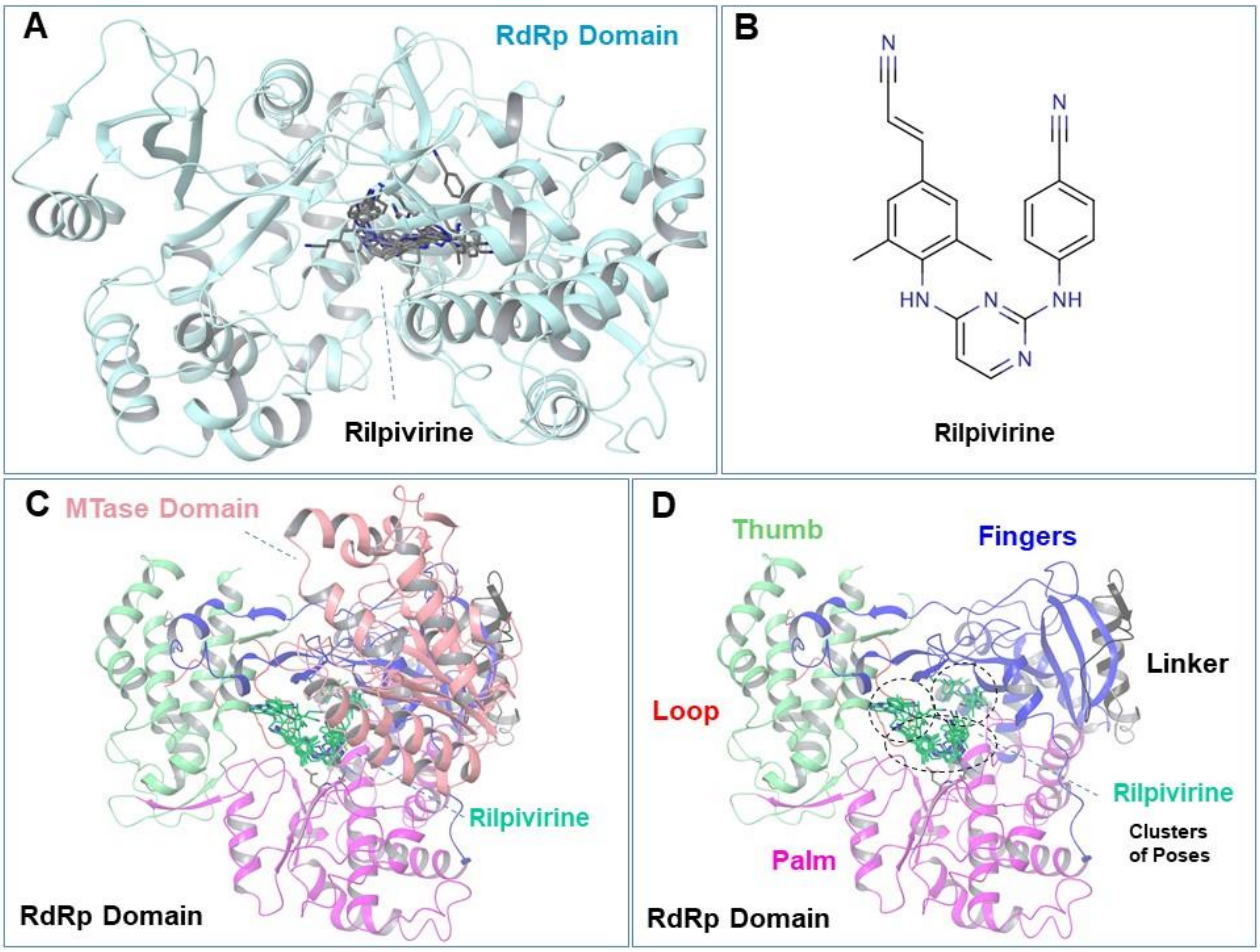

Supplemental Figure 6: Putative binding mode of RPV at the Palm Site, RdRp Domain. The structure of ZIKV NS5 is shown in New Cartoon representation, in light blue color (A) or colored according to different RdRp subdomains (finger, palm, thumb, linker and loop colored in blue, magenta, green, black and red, respectively). A-D. Docking modes of RPV (green carbons) are shown. Binding conformations of RPV at this site cluster into three distinct conformations. In A, RPV is shown in gray carbons; in C-D in green carbons. B. 2D sketch of RPV. B-D. Critical binding interactions are shown. In C, RPV is superimposed to complementary site map features (yellow: hydrophobic, red and blue: ligand acceptor and donor maps).

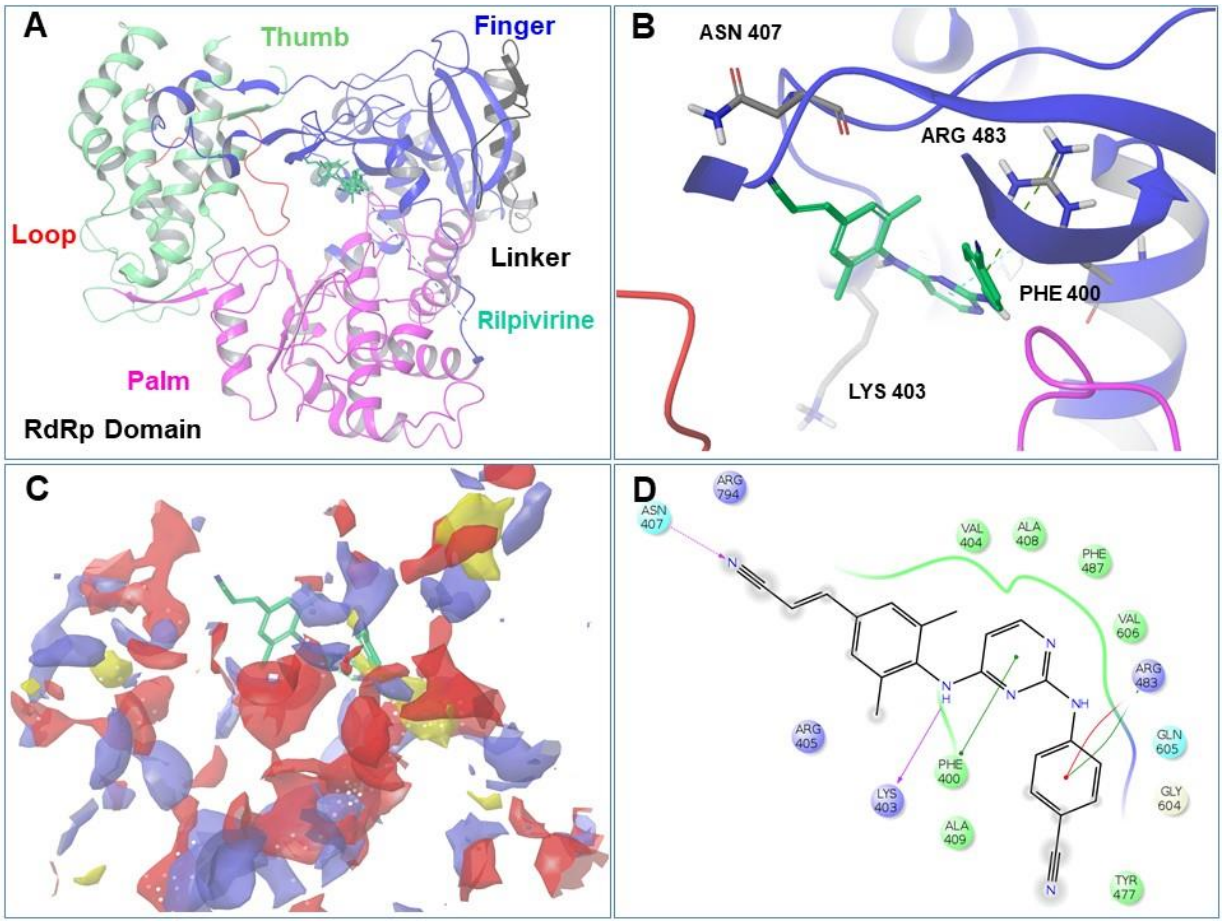

Supplemental Figure 7: Putative binding mode of RPV at the Palm Site, finger sub-domain.

The structure of ZIKV NS5 is shown in New Cartoon representation; finger, palm, thumb, linker and loop sub-domains are colored in blue, magenta, green, black and red, respectively. A. A cluster of docking modes of RPV (green carbons) is shown. B-D. Critical binding interactions are shown. In C, RPV is superimposed to complementary site map features (yellow: hydrophobic, red and blue: ligand acceptor and donor maps).

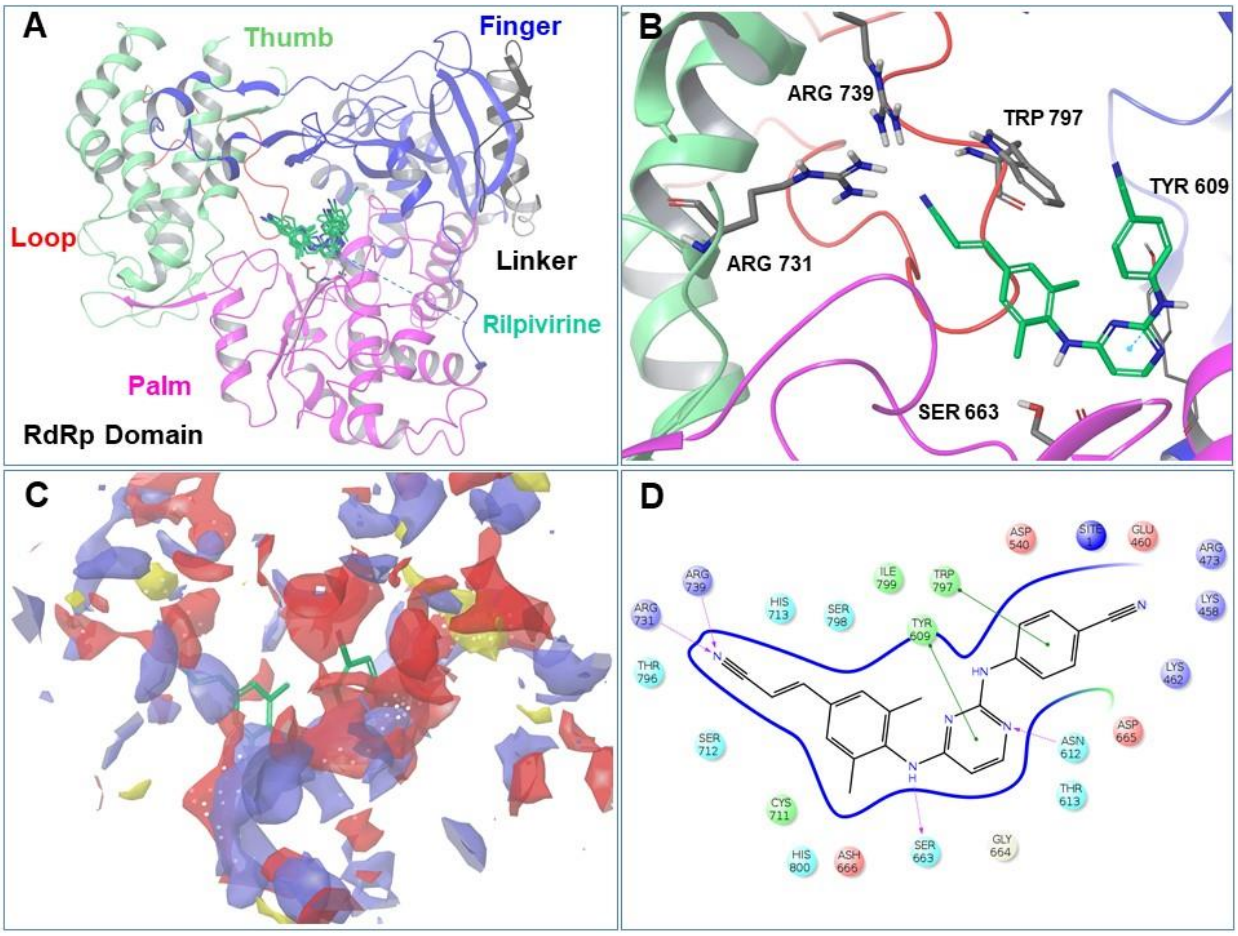

Supplemental Figure 8: Putative binding mode of RPV at the Palm Site, palm sub-domain. The structure of ZIKV NS5 is shown in New Cartoon representation; finger, palm, thumb, linker and loop sub-domains are colored in blue, magenta, green, black and red, respectively. A. A cluster of docking modes of RPV (green carbons) is shown. B-D. Critical binding interactions are shown. In C, RPV is superimposed to complementary site map features (yellow: hydrophobic, red and blue: ligand acceptor and donor maps).

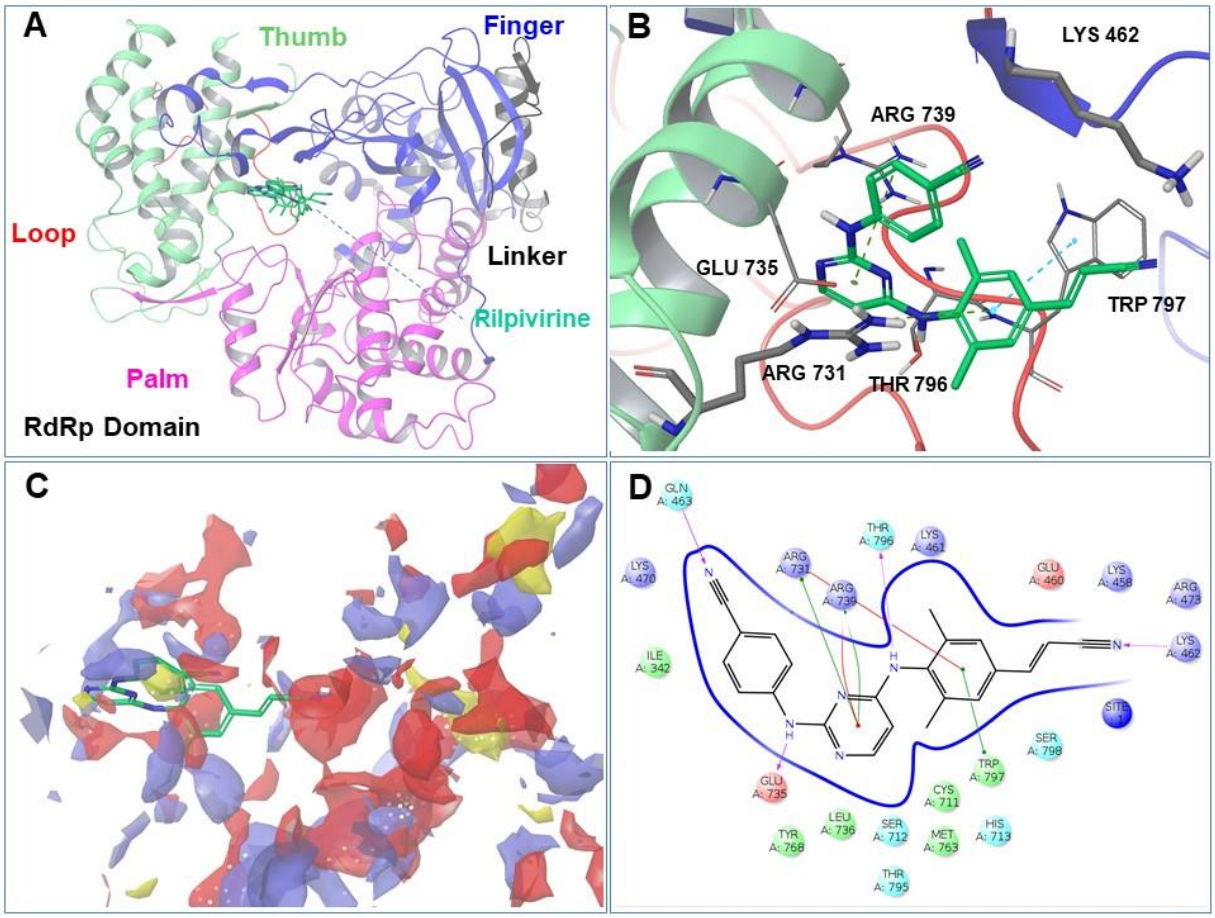

Supplemental Figure 9: Putative binding mode of RPV at the Palm Site, thumb sub-domain. The structure of ZIKV NS5 is shown in New Cartoon representation; finger, palm, thumb, linker and loop sub-domains are colored in blue, magenta, green, black and red, respectively. A. A cluster of docking modes of RPV (green carbons) is shown. B-D. Critical binding interactions are shown. In C, RPV is superimposed to complementary site map features (yellow: hydrophobic, red and blue: ligand acceptor and donor maps).

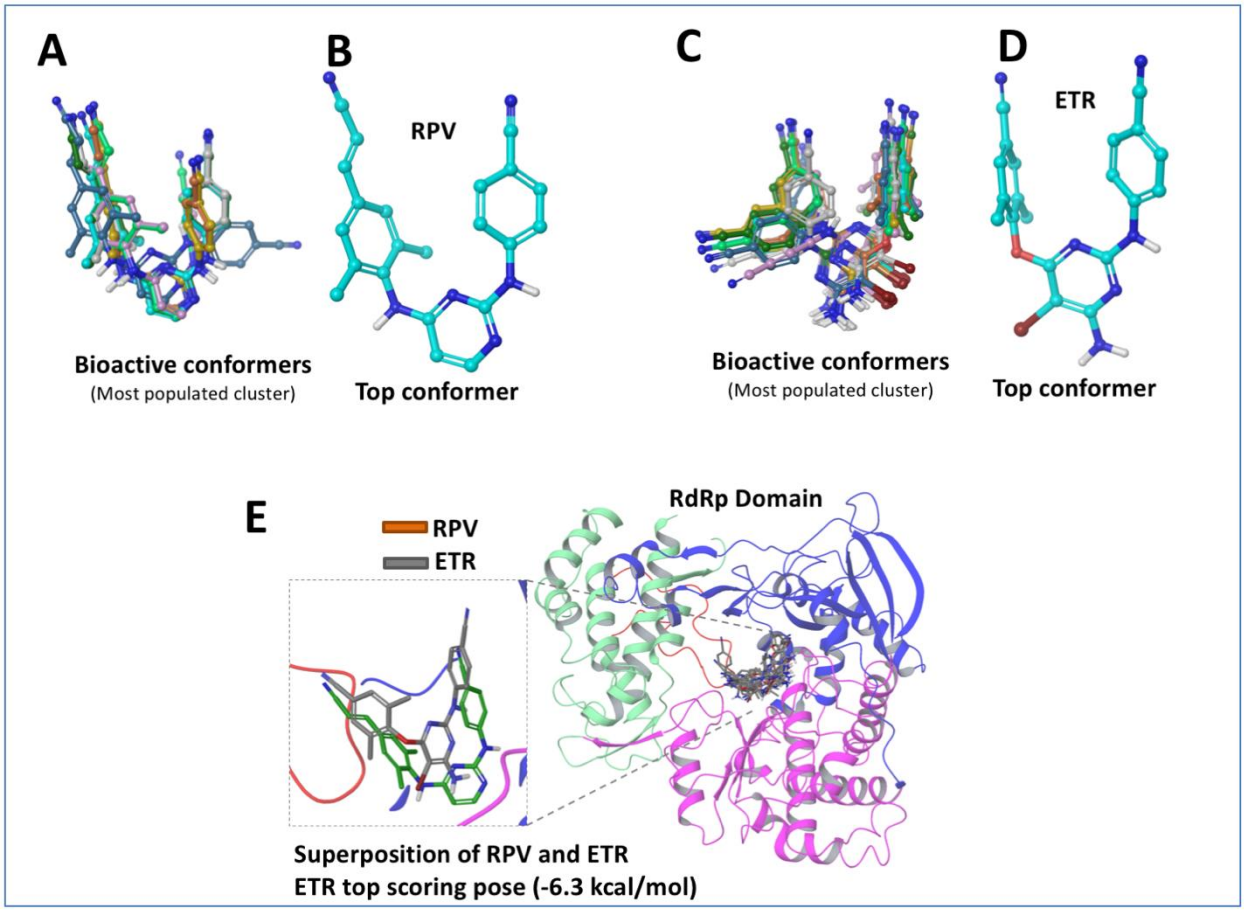

Supplemental Figure 10: Bioactive conformation and best predicted binding of RPV to the RdRp Domain of NS5. Most populated cluster of conformers of RPV (A) and top conformer (B). Bioactive conformation and predicted binding of ETR to the RdRp Domain of NS5 (compared to RPV). Most populated cluster of conformers of ETR (C) and top conformer (D). Binding mode of ETR to the NS5 RdRp domain (E), generated by molecular docking, is compared a representative binding mode of RPV. In all cases, both ETR and RPV adopts the “horseshoe” binding conformation that was previously observed in the experimental complex of RPV bound to HIV-1 RT (*).

(*) Das, K. et al. High-resolution structures of HIV-1 reverse transcriptase/TMC278 complexes: Strategic flexibility explains potency against resistance mutations. Proc. Natl. Acad. Sci. 105, 1466 (2008).

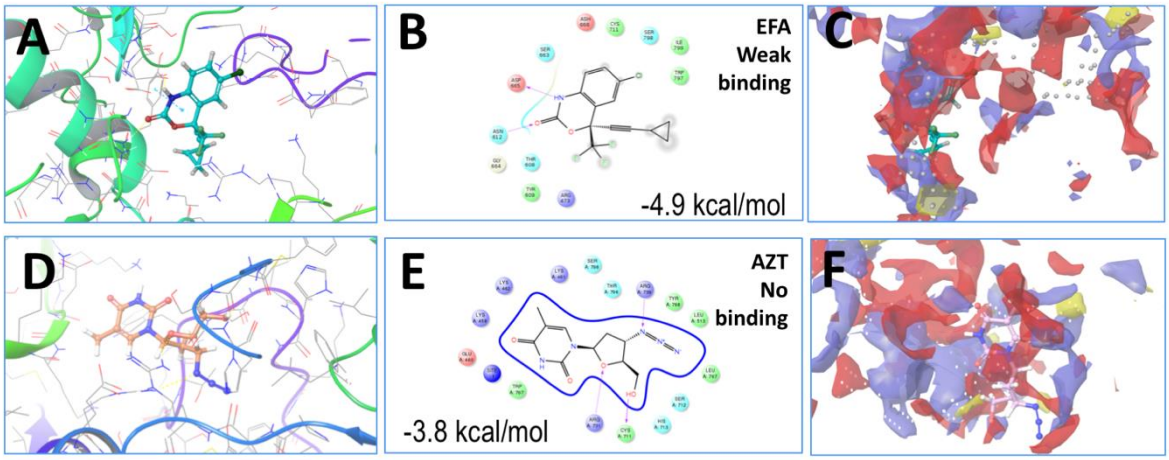

Supplemental Figure 11: Predicted binding modes of the NNRTI EFA and the NRTI AZT to the RdRp domain of NS5. Docking scores are indicated in parenthesis and correlate with experimental data showing that, while the inhibitory effect of EFA could only be detected at high concentrations (suggesting weak binding), AZT did not interfere at all (suggesting no binding) with NS5 activity (Fig. 2, panels B and D).

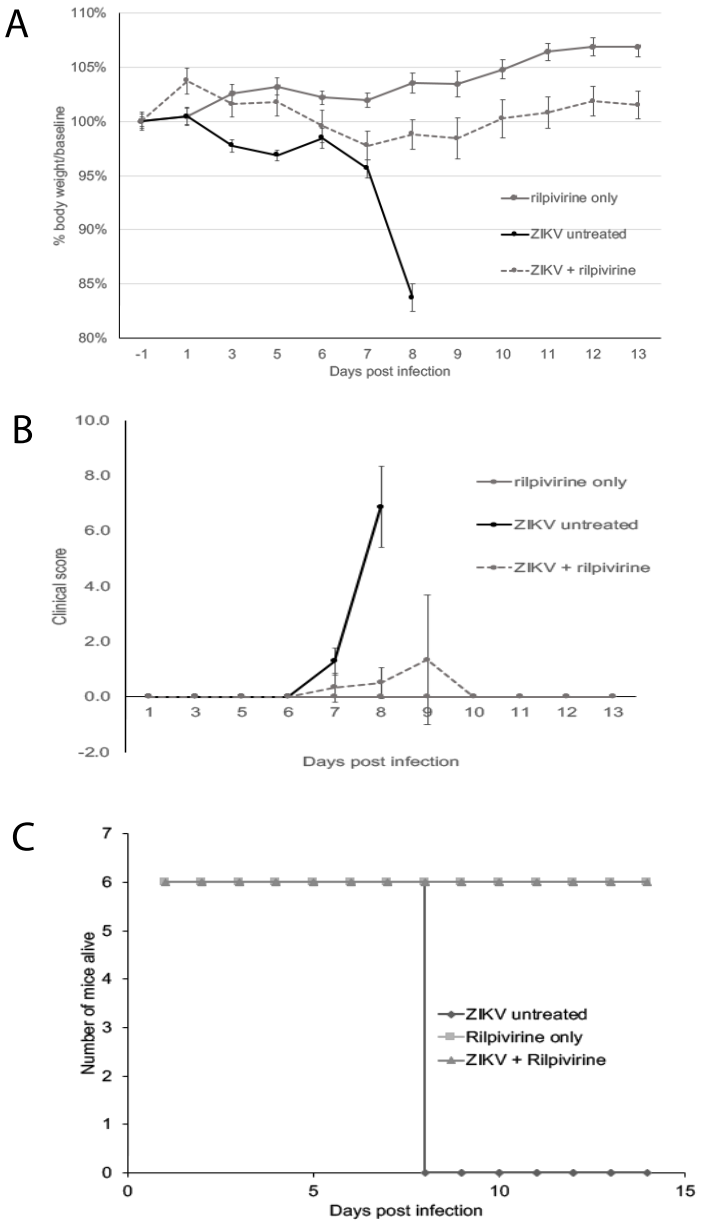

Supplemental Figure 12: RPV reverses the mortality and decreases the viral burden in the IFNR$^{-/-}$ mice. Eighteen IFNR knockout transgenic (IFNR$^{-/-}$) mice, obtained from Jackson laboratories, at four months were divided into three groups; 1. RPV treatment and mock infection (n=6), 2. ZIKV infection, no treatment (n=6), and 3. RPV treatment and ZIKV infection (n=6).

twelve animals were started treatment with RPV two days prior ZIKV or mock infection. RPV treatments were continued daily. Twelve mice were infected with PRVABC59 strain of ZIKV and six with a mock infection (PBS only) through footpad injections. **A.** Body weights were measured for each mouse from the three groups (closed square-rilpivirine only; closed circle- ZIKV untreated; open triangle- ZIKV + RPV) until the end of the study (14 days post infection (dpi)). Data are shown as a percent of body weight compared to baseline. **B.** Grasp tests were performed daily starting at 4 dpi and analyzed for clinical scoring for the three groups. **C.** Survivor curve analysis is shown based on the Kaplan-Meier estimates. All animals in the RPV only and ZIKV + RPV groups survived until the end of the study. The ZIKV mice were sacrificed at 8 dpi.

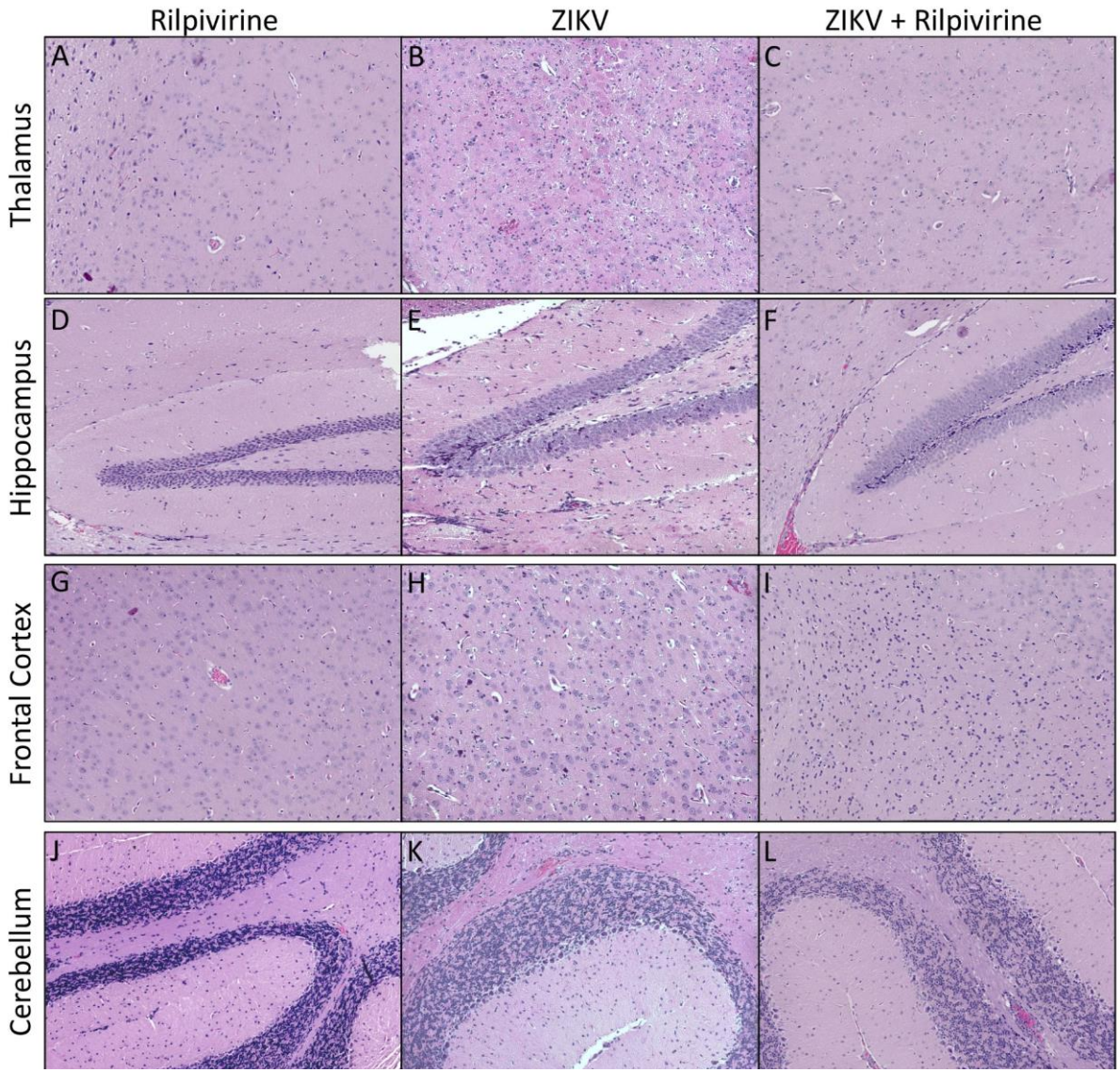

Supplemental Figure 13: Significant inflammation and necrosis with ZIKV in the brains of IFNR$^{-/-}$ infected mice. Thalamus (**A-C**), hippocampus (**D-F**), frontal cortex (**G-I**) and cerebellum (**J-L**) from RPV only (RPV) **(A, D, G, J)**, ZIKV-infected animals (ZIKV) **(B, E, H, K)** and ZIKV - infected, RPV-treated animals (ZIKV + RPV) **(C, F, I, L)** were stained with hematoxylin and eosin. **(A, D, G, J)**. The rilpivirine-only control brains were unremarkable. **(B, E, H, K)**. All brain regions (thalamus, hippocampus, frontal cortex and cerebellum) examined in the ZIKV only mice had significant inflammation, but also abundant apoptotic/necrotic cell damage. **(C, F, I, L)**. In the RPV

treated ZIKV infected animals, there was still significant inflammation, but no apoptotic/necrotic cell damage was seen.

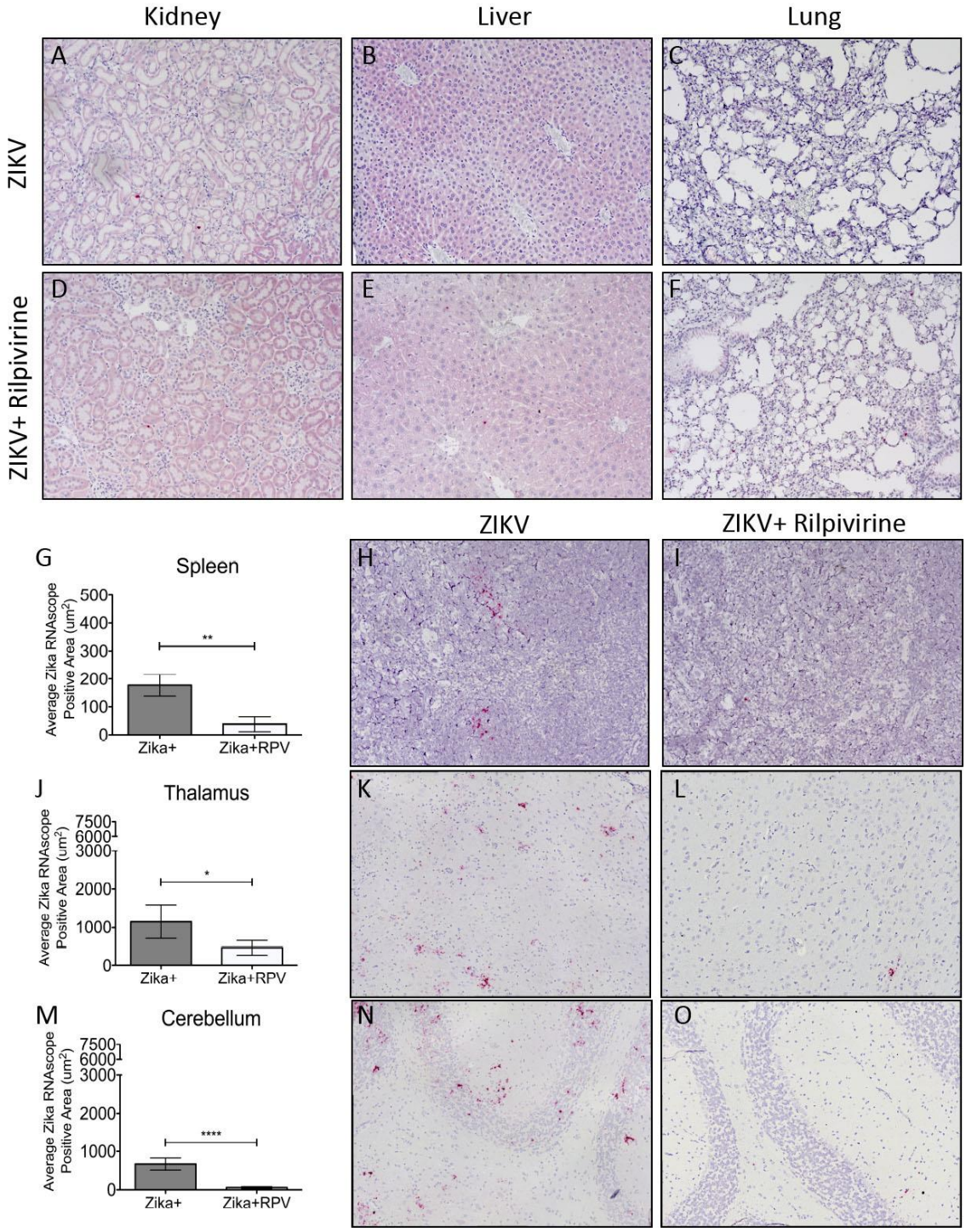

Supplemental Figure 14: Comparison of ZIKV RNA in kidney, liver, lungs, spleen, thalamus and cerebellum. ZIKV RNA was visualized with RNAscope (red) in kidney **(A-B)**, liver **(C-D)**, and lungs **(E-F)** of ZIKV-infected animals (ZIKV) and ZIKV -infected, RPV-treated animals (ZIKV

+ RPV). **(G)** Quantitation of ZIKV RNA in spleen showed low levels of ZIKV RNA in the ZIKV infected animals (176.8 ± 39.1 μm^2), which significantly decreased with RPV treatment (38.0 ± 26.7 μm^2) (P<.001). **(H)** Representative image of a spleen ZIKV RNAScope in situ reveals high viral RNA signal in ZIKV mice. **(I)** Representative image of spleen ZIKV RNAScope staining shows few ZIKV RNA+ cells in ZIKV + RPV mice. **(J)** Quantitation of ZIKV RNA in thalamus showed moderate levels of ZIKV RNA in the ZIKV infected animals (1149.3 ± 440.7 μm^2), which significantly decreased with RPV treatment (464.8 ± 193.5μm^2) (P<.05). **(K**) Representative image of a thalamus ZIKV RNAScope in situ reveals moderate viral RNA signal in ZIKV mice. **(L)** Representative image of thalamus ZIKV RNAScope staining shows decreased ZIKV RNA+ cells in ZIKV + RPV mice. **(M)** Quantitation of ZIKV RNA in cerebellum showed moderate levels of ZIKV RNA in the ZIKV infected animals (669.9 ± 157.9 μm^2), which significantly decreased with RPV treatment (56.4 ± 25.0 μm^2) (P<.05). **(N)** Representative image of a cerebellum ZIKV RNAScope in situ reveals moderate viral RNA signal in ZIKV mice. **(O)** Representative image of cerebellum ZIKV RNAScope staining shows decreased ZIKV RNA+ cells in ZIKV + RPV mice. The average Zika RNA signal area was quantitated as the average of 10, non-overlapping 40X images from each animal (n=3/group), using a Keyence BZ-X700 microscope. Bar graphs show average Zika RNA area (mean, SEM). Comparison of means was determined by Mann-Whitney, two-tailed t-test. (*P<0.05, ****P<0.0001)